

# KOLMOGOROV-ARNOLD ENERGY MODELS: FAST AND INTERPRETABLE GENERATIVE MODELING

**Prithvi Raj**

The Zettascale Computing Corp. \*  
prithvi@zscc.ai

## ABSTRACT

Learning an energy-based model (EBM) in the latent space of a top-down generative model offers a powerful framework for generation across many data modalities. However, it remains unclear how its interpretability can be used to guide model design, improve generative quality, and reduce training time. Moreover, the reliance on Langevin Monte Carlo (LMC) sampling presents challenges in efficiency and sampling multimodal latent distributions. We propose a novel adaptation of the Kolmogorov-Arnold representation theorem for generative modeling and introduce the Kolmogorov-Arnold Energy Model (KAEM) to take advantage of structural and inductive biases. By constraining the prior to univariate relationships, KAEM enables fast and exact inference via the inverse transform method. With the low dimensionality of the latent space and suitable inductive biases encoded, we demonstrate that importance sampling (IS) becomes a viable, unbiased, and highly efficient posterior sampler. For domains where IS fails, we introduce a strategy based on population-based LMC, decomposing the posterior into a sequence of annealed distributions to improve LMC mixing. KAEM balances common generative modeling trade-offs, offering fast inference, interpretability, and stable training, while being naturally suited to Zettascale Computing hardware.

## 1 INTRODUCTION

Deep generative modeling is a core subfield of machine learning that enables systems to learn complex data distributions, generate novel data, and support a wide range of tasks including simulation, compression, and representation learning. Two prominent and widely studied approaches are Variational Autoencoders (VAEs) (Kingma & Welling, 2022) and Generative Adversarial Networks (GANs) (Goodfellow et al., 2014). Both frameworks assume that each data point is generated from a low-dimensional latent vector via a top-down neural network, where the latent vector is typically drawn from a simple, non-informative prior, such as a uniform or isotropic Gaussian distribution.

Latent energy-based prior models (EBMs) (Pang et al., 2020) extend this framework by learning an expressive, data-dependent prior directly in the latent space. This prior can be trained jointly with the top-down generator using maximum likelihood estimation (MLE), where the EBM learns by the statistical discrepancy between samples from the prior and posterior distributions, following a paradigm similar to Empirical Bayes. Each learning iteration requires Markov Chain Monte Carlo (MCMC) sampling from both the prior and posterior, specifically the Unadjusted Langevin Algorithm (ULA) (Brooks et al., 2011; Rossky et al., 1978b; Roberts & Stramer, 2002), which often offers greater modeling flexibility compared to the amortized inference methods of VAEs.

Despite being extendable to several high-impact research directions, such as multimodal generative modeling (Yuan et al., 2024), and interpretable classification, text-to-text, and meta-learning (Kong et al., 2021), (which involves rapid adaptability and few-shot generalization to out-of-distribution tasks), latent EBMs face critical limitations due to their reliance on MCMC sampling.

Firstly, MCMC is inherently iterative, and algorithms such as ULA require repeated gradient passes through the model, which introduces significant computational overhead during both training and inference. Secondly, ULA is best suited for sampling from smooth, unimodal distributions and can

---

\*Previously Exa Laboratories

struggle to explore the multimodal latent distributions that are typical in latent variable generative modeling. Moreover, the framework presented by Pang et al. (2020) requires separate ULA samplers for the prior and posterior. This introduces additional experimental complexity since ULA is sensitive to hyperparameter tuning: step sizes that are too small lead to poor mixing and convergence, while larger step sizes can accumulate discretization bias due to its use of the Euler-Maruyama method (Wilkie, 2004) to evolve the underlying Langevin equation.

Additionally, it is unclear how the unique separation between the prior and generator networks can be leveraged for interpretability or training efficiency. Unlike the framework introduced by Karniadakis et al. (2021), which describes how scientific inductive and learning biases can be embedded into neural networks to reduce their reliance on data and improve training efficiency, generalization, and explainability, (all of which are critical for ensuring trust in Artificial Intelligence), it remains unclear how the EBM prior can be effectively aligned with the posterior to achieve similar effects. Although ideas from mechanistic interpretability, as reviewed by Bereska & Gavves (2024), could potentially be applied, there is currently no established method to leverage the unique strengths of the EBM prior framework for this purpose.

### 1.1 INDUCTIVE BIASES AND FAST SAMPLING

To address these limitations, we reimagine the EBM prior into a novel univariate or element-wise model, drawing inspiration from Kolmogorov-Arnold Networks (KANs) (Liu et al., 2024) and deep spline networks Bohra et al. (2020), which replace the sigmoidal activations used in multilayer perceptrons Murtagh (1991) with spline interpolations. By representing the latent space with univariate functions and distributions, we enable fast, (single forward pass), and exact prior sampling with the inverse transform method (Devroye, 1986) and improve interpretability for domain experts who may not be deeply familiar with machine learning. This allows the EBM prior to be aligned with the posterior before training begins, and for latent distributions to be plotted, viewed, and potentially understood with the symbolic regression approach proposed by Liu et al. (2024).

In Sec. 3.1, we show that simple datasets can allow for efficient training with importance sampling (IS) (Goertzel, 1949). This is a technique for estimating posterior expectations that is otherwise avoided in the literature due to its high variance under severe prior-posterior mismatch and the curse of dimensionality, (Dupuis & Wang, 2004), which can be avoided in our model due to the low dimensionality of the latent space. Moreover, we show that the trained priors are easy to visualize and recover, offering new opportunities for latent discovery and knowledge transfer to models with different latent structures.

To derive our new model, which we call the Kolmogorov-Arnold Energy Model (KAEM), we first introduce a novel adaptation of the Kolmogorov-Arnold Representation Theorem (KART) (Givental et al., 2009) by reinterpreting its inner functions as Markov kernels between probability spaces. Given its finite and definitive nature, KART can provide structural bias and reduce the reliance of architecture design on intuition and automated tuning.

This reinterpretation allows us to frame inverse transform sampling (ITS) as a measurable transformation applied to uniform noise, thus preserving the deterministic structure of KART while admitting a probabilistic interpretation that aligns with MLE. To address the potential inflexibility of strict adherence to KART and the limitations of using independent energy-based priors, we introduce a scalable strategy based on mixture distributions. Beyond introducing dependencies between latent dimensions to capture inter-dimensional relationships, this also improves sampling efficiency by enabling component-wise sampling.

## 1.2 POPULATION-BASED LANGEVIN SAMPLING AND THERMODYNAMIC TRAINING

However, while ITS enables fast inference, posterior sampling must still be conducted using ULA when the IS estimator is rendered ineffective due to variance. Prior work addressing poor MCMC convergence and multimodal exploration in EBMs has typically relied on diffusion models, such as the hierarchical EBM by Cui & Han (2024) and the diffusion-assisted EBM by Zhang et al. (2023).

To maintain prior interpretability and fast inference post-training, we instead introduce posterior annealing as a novel and alternative strategy. This involves decomposing the posterior into a sequence of power posteriors, presented by Friel & Pettitt (2008), and recasting ULA with population-based MCMC methods (Swendsen & Wang, 1986; Marinari & Parisi, 1992; Hukushima & Nemoto, 1996).

The training criterion is derived from the discretized Thermodynamic Integral and the Steppingstone Estimator (SE), as presented by Calderhead & Girolami (2009); Annis et al. (2019) to ensure the impact of annealing on learning dynamics and parameter updates. Although this might be less expressive than hierarchical EBMs, it ensures that inductive biases remain easy to embed into the latent prior and interpret after training; and unlike denoising, which scales sequentially, annealing can scale by adding more annealed distributions in parallel.

While ULA is computationally efficient and enables more flexible chain dynamics, it does not preserve detailed balance or reversibility. This can be recovered by incorporating Metropolis-Hastings (MH) adjustments (Metropolis & Ulam, 1949) via the Metropolis-adjusted Langevin Algorithm (MALA) (Rosky et al., 1978a). However, ULA remains the preferred method in our work, motivated by its efficiency and effectiveness, demonstrated by Pang et al. (2020) and further supported by the findings of Nijkamp et al. (2019b;a), with regards to how short-run, biased MCMC methods can still be highly effective for sampling from EBMs.

MLE and SE are compared in Sec. 3.2. Despite our optimizations, the element-wise and localized nature of KANs complicate their parallelization on GPUs, which are best suited to matrix arithmetic. As a result, forward passes through KAEM and the gradient evaluations required for ULA were found to be slow, necessitating reduced experimental complexity.

## 1.3 SCOPE OF EXPERIMENTS

KAEM was compiled and differentiated using Julia’s Reactant (EnzymeAD & Reactant.jl Contributors, 2025) and Enzyme (Moses & Churavy, 2020; Moses et al., 2021; 2022) packages, which optimizes and lowers Julia code to Multi-Level Intermediate Representation (MLIR) (Lattner et al., 2020), thus offering best-in-class performance. However, Gaussian Radial Basis Functions (RBF KANs) (Li, 2024), were adopted instead of the cubic B-spline bases proposed by Liu et al. (2024), as RBFs are Reactant-compatible and more efficient for GPU implementation. They have also been proven to provide an optimal solution to the regularized approximation/interpolation problem by Poggio & Girosi (1990).

The experiments in Sec. 3.2 demonstrate that our mixture prior model is able to generate coherent, (although low-quality), samples after a few training epochs on RGB images, while still supporting efficient, exact sampling via component-wise ITS. In contrast, annealing incurred substantial computational overhead, but produced small improvements in sample quality, rendering its recommendation context-dependent. However, this may change as a larger number of power posteriors, longer training durations, and more advanced posterior sampling algorithms become practical with the hardware advances proposed by Zetta (2024). Their architecture enables fine-grained control over data flow and parallelized element-wise nonlinearity which is naturally well suited to supporting KAEM at scale. Their XPU’s also provide function/layer fusion capabilities that may improve the potential of univariate priors and adherence to KART.

We present KAEM as an initial step to inspire further adaptations of KART in machine learning. This work aims to lay the groundwork for more exploration amongst the research community, with the far-reaching hope of eventually advancing towards a broader conceptualization: *“The Kolmogorov-Arnold Representation Theorem Is All You Need.”*

## 2 THE KOLMOGOROV-ARNOLD ENERGY MODEL

This section introduces the model and its associated sampling procedures. We begin by presenting a novel interpretation of the Kolmogorov-Arnold Representation Theorem (KART) to define the model’s baseline architecture. Our key practical contribution is the introduction of a univariate energy-based prior, detailed in Sec. 2.1. The top-down generator can be instantiated in various forms, including Kolmogorov-Arnold Networks (KANs), which enables strict adherence to KART.

We then propose scalable extensions to the model, including mixture distributions in Sec. 2.3.2, which introduce dependencies between latent dimensions. This represents a novel contribution to the literature on EBM priors. The final sections address prior and posterior sampling: we introduce inverse transform sampling (ITS) as a new approach for efficient EBM prior sampling, and introduce the posterior annealing strategy in Sec. 2.5 to improve multimodal sampling during training.

The Kolmogorov-Arnold Representation theorem (KART) (Givental et al., 2009) forms the basis of KAEM. A structured proof of the theorem has been provided by Dzhenzher & Skopenkov (2022).

**The Kolmogorov-Arnold Representation theorem 1** *For any integer  $n_z > 1$ , there are continuous univariate functions  $\Phi_q : \mathbb{R} \rightarrow \mathbb{R}$  and  $\psi_{q,p} : [0, 1] \rightarrow \mathbb{R}$ , such that any continuous multivariate function,  $g : [0, 1]^{n_z} \rightarrow \mathbb{R}$ , can be represented as a superposition of those functions:*

$$g(u_1, \dots, u_{n_z}) = \sum_{q=1}^{2n_z+1} \Phi_q \left( \sum_{p=1}^{n_z} \psi_{q,p}(u_p) \right), \quad (1)$$

Eq. 1 can provide structural bias and guide the design of KAEM’s architecture. To ensure adherence to it, any transformations must be derived to be continuous, measurable, and deterministic. For readers less familiar with the technical background, the two most practically significant equations of Sec. 2.1 are Eqs. 4 & 6.

### 2.1 UNIVARIATE ENERGY-BASED PRIOR

The functions  $\psi_{q,p}$  can be conveniently translated to the framework of inverse transform sampling (ITS) (Devroye, 1986). We interpret  $\psi_{q,p}$  as the application of an inverse cumulative density function (CDF) to a uniform random variable to recover a sample from a univariate latent density,  $p_{q,p}$ :

$$z_{q,p} = \psi_{q,p}(u_p) = F_{\pi_{q,p}}^{-1}(u_p) \Leftrightarrow z_{q,p} \sim p_{q,p}(z). \quad (2)$$

Here,  $F_{\pi_{q,p}}^{-1} : [0, 1] \rightarrow \mathcal{Z}_{q,p}$  is the generalized inverse CDF associated with a parameterized latent measure,  $\pi_{q,p}$  in the latent space,  $\mathcal{Z}_{q,p} \subset \mathbb{R}$ . We have therefore interpreted  $u_p \sim \text{Unif}(0, 1)$  in Eq. 1 as a uniform random variable in the probability space,  $([0, 1], \mathcal{B}([0, 1]), \mu)$ , where  $\mathcal{B}([0, 1])$  is the Borel  $\sigma$ -algebra on  $[0, 1]$  and  $\mu$  is the uniform probability measure on  $[0, 1]$ .

This is valid under standard regularity assumptions on  $F$ , since it is a measurable, monotone, increasing function, and thus  $F_{\pi_{q,p}}^{-1}(u) = \inf \{z \in \mathcal{Z}_{q,p} : F_{\pi_{q,p}}(z) \geq u\}$  is a measurable pushforward (or Markov kernel) between the two probability spaces:

$$([0, 1], \mathcal{B}([0, 1]), \mu) \xrightarrow{F_{\pi_{q,p}}^{-1}} (\mathcal{Z}_{q,p}, \mathcal{B}(\mathcal{Z}_{q,p}), \pi_{q,p}), \quad (3)$$

We parameterize the latent measure  $\pi_{q,p}$  via exponential tilting of a base measure  $\pi_0$ :

$$d\pi_{q,p}(z) = \frac{\exp(f_{q,p}(z))}{Z_{q,p}} d\pi_0(z), \quad (4)$$

where  $f_{q,p}(z)$  is a learned energy function and  $Z_{q,p}$  is the finite normalizing constant (partition function) that ensures  $\pi_{q,p}$  induces a valid probability density,  $p_{q,p}$ , for each latent feature.

The inspiration for this exponential tilting form can be traced to the energy-based prior introduced by Pang et al. (2020), adapted to the univariate case. The base prior  $\pi_0$  serves as a reference that

guides the form of the learned  $\pi_{q,p}$ , allowing for flexible reweighting via the energy function  $f_{q,p}$ . For  $\pi_{q,p}$  to define a valid density, which we denote  $p_{q,p}$ , we require exponential integrability:

$$\begin{aligned} \exp(f_{q,p}(z)) &\in L^1(\pi_0) \\ \text{such that } Z_{q,p} &= \int_{\mathcal{Z}_{q,p}} \exp(f_{q,p}(z)) \pi_0(dz) < \infty. \end{aligned} \quad (5)$$

In practice,  $f_{q,p}$  can be parameterized in various ways, made possible by the recent development of Kolmogorov-Arnold Networks (KANs) (Liu et al., 2024). For instance, smoothing splines, such as those used by KANs or deep spline networks, (Bohra et al., 2020). Splines are typically defined on bounded domains, allowing the support of  $\pi_{q,p}$  to be explicitly controlled by the user using the KAN grids. These grids must be periodically updated during training according to input activations, following the implementation described by Liu et al. (2024).

The partition function  $Z_{q,p}$  is often intractable in energy-based models. However, in this univariate setting, where the energy function is smooth and defined on a bounded domain  $[z_{\min}, z_{\max}]$ , it can be accurately approximated using Gauss-Kronrod quadrature, (Laurie, 1997):

$$Z_{q,p} = \int_{z_{\min}}^{z_{\max}} \exp(f_{q,p}(z)) \pi_0(z) dz \approx \sum_{i=1}^{N_{\text{quad}}} w_i G(z_i^{\text{node}}), \quad (6)$$

where  $G(z) = \exp(f_{q,p}(z)) \pi_0(z)$ , and  $\{z_i^{\text{node}}, w_i\}_{i=1}^{N_{\text{quad}}}$  are the quadrature nodes and weights for the interval  $[z_{\min}, z_{\max}]$ . The availability of  $Z_{q,p}$  enables ITS, and the smoothness of  $G$ , together with its bounded support, makes this approximation accurate.

With this valid form for the normalized CDF, inverse transform sampling (ITS) can be used to draw samples from  $p_{q,p}$  as measurable transformations of uniform noise. This preserves the deterministic structure of KART while enabling flexible, learnable latent distributions, well-founded so long as the KAN functions admit exponential integrability.

As a result, the model retains a coherent probabilistic interpretation of KART that is consistent with the energy-based framework proposed by Pang et al. (2020), which is well suited to maximum likelihood training. However, this approach is significantly limited, as it ignores inter-dimensional dependencies in the latent space and results in an axis-aligned joint distribution. We address this inflexibility in Sec. 2.3.2 by relaxing our adherence to KART.

### 2.1.1 MULTIVARIATE PRIOR NOTATION

From this point forward, we formulate our derivations over the multivariate probability space,  $(\mathcal{Z}, \mathcal{B}(\mathcal{Z}), \mathbb{P}_\theta)$ , where  $\mathbb{P}_\theta$  denotes a product measure parameterized by abstract model parameters,  $\theta$ , and the latent space is defined as a Cartesian product:

$$\mathbb{P}_\theta := \bigotimes_{q=1}^{2n_z+1} \bigotimes_{p=1}^{n_z} \pi_{q,p}, \quad \mathcal{Z} = \prod_{q=1}^{2n_z+1} \prod_{p=1}^{n_z} \mathcal{Z}_{j,k} \subset \mathbb{R}^{(2n_z+1) \times n_z}, \quad (7)$$

Each  $\pi_{q,p}$  is a univariate probability measure on  $\mathcal{Z}_{q,p}$  defined via exponential tilting, as introduced in Eq. 4. Under  $\mathbb{P}_\theta$ , the latent variables  $\{z_{q,p}\}_{q,p}$  are mutually independent, and the full latent variable

$$\mathbf{z} = (z_{q,p})_{q=1, \dots, 2n_z+1; p=1, \dots, n_z}$$

is a matrix-valued random variable whose entries correspond to independent univariate features.

## 2.2 KOLMOGOROV-ARNOLD NETWORK GENERATOR

Having sampled the intermediary latent variable with ITS such that  $z_{q,p} = F_{\pi_{q,p}}^{-1}(u_p)$ , the generator can be realized flexibly as  $\mathcal{G} : \mathcal{Z} \rightarrow \mathcal{X}$ :

$$\tilde{\mathbf{x}}^{(s)} = \mathcal{G}(\mathbf{z}^{(s)}) + \boldsymbol{\epsilon}^{(s)}, \quad \text{where } z_{q,p}^{(s)} \sim p_{q,p}(z), \quad \boldsymbol{\epsilon}^{(s)} \sim \mathcal{N}(\mathbf{0}, \sigma_\epsilon^2 \mathbf{I}), \quad (8)$$

where  $\tilde{\mathbf{x}}^{(s)} = \{\tilde{x}_o^{(s)}\}_{o=1}^{n_x}$  represents a generated data sample corresponding to a single latent sample indexed by  $s$ , and  $n_x$  is used to specify the dimension of  $\tilde{\mathbf{x}}^{(s)}$ . The additive noise is a Gaussian

sample with hyperparameter  $\sigma_\epsilon$ . However, the architecture may be made strictly adherent to KART using a Kolmogorov-Arnold Network:

$$\tilde{x}_o^{(s)} = \sum_{q=1}^{2n_z+1} \Phi_{o,q} \left( \sum_{p=1}^{n_z} z_{q,p}^{(s)} \right) + \epsilon_o^{(s)}, \quad \tilde{\mathbf{x}}^{(s)} = \begin{pmatrix} \sum_{q=1}^{2n_z+1} \Phi_{1,q} \left( \sum_{p=1}^{n_z} z_{q,p}^{(s)} \right) \\ \sum_{q=1}^{2n_z+1} \Phi_{2,q} \left( \sum_{p=1}^{n_z} z_{q,p}^{(s)} \right) \\ \vdots \\ \sum_{q=1}^{2n_z+1} \Phi_{n_x,q} \left( \sum_{p=1}^{n_z} z_{q,p}^{(s)} \right) \end{pmatrix} + \boldsymbol{\epsilon}^{(s)}. \quad (9)$$

The functions,  $\Phi_{o,q} : \mathbb{R} \rightarrow \mathbb{R}$ , are realizable as basis or KAN functions similar to  $f_{q,p} : \mathcal{Z}_{q,p} \rightarrow \mathbb{R}$ .

### 2.3 SCALING KAEM

The trainable components of the prior and inner functions are shared across the features of each input  $\mathbf{x}^{(b)}$ , while the outer generator functions remain separate for each output dimension. Specifically, the learnable functions are defined as:

$$\mathbf{f} = \begin{pmatrix} (f_{1,1}, \dots, f_{1,n_z}) \\ (f_{2,1}, \dots, f_{2,n_z}) \\ \vdots \\ (f_{2n_z+1,1}, \dots, f_{2n_z+1,n_z}) \end{pmatrix}, \quad \boldsymbol{\Phi} = \begin{pmatrix} (\Phi_{1,1}, \dots, \Phi_{1,2n_z+1}) \\ (\Phi_{2,1}, \dots, \Phi_{2,2n_z+1}) \\ \vdots \\ (\Phi_{n_x,1}, \dots, \Phi_{n_x,2n_z+1}) \end{pmatrix}, \quad (10)$$

where  $n_x$  denotes the dimensionality of the observed data.

#### 2.3.1 GENERATOR

The generator,  $\mathcal{G}$ , can be considered a separate generator network allowing for more flexible realizations, such as convolutional layers when adherence to Eq. 1 is not required. Deepening this generator, as guided by Liu et al. (2024) for the Kolmogorov-Arnold Network (KAN), does not replace KART as the innermost foundation of KAEM:

$$x_o^{(s)} = \sum_{l_n=1}^{L_n} h_{o,l_n} \left( \dots h_{l_3,l_2} \left( \sum_{l_1=1}^{L_1} h_{l_2,l_1} \left( \sum_{q=1}^{2n_z+1} \Phi_{l_1,q} \left( \sum_{p=1}^{n_z} z_{q,p}^{(s)} \right) \right) \right) \right) + \epsilon_o^{(s)}. \quad (11)$$

Here, each  $h$  represents a hidden layer introduced between the outer sum of Eq. 1, and the output feature space to allow for more expressivity when required. In fact, each successive instance of  $h$  can be interpreted as a distinct outer sum of Eq. 1, where the inner sum corresponds to the previous layer. This is valid provided that:

$$L_1 = 2(2n_z + 1) + 1, \quad L_2 = 2L_1 + 1, \quad \dots \quad L_n = 2L_{n-1} + 1. \quad (12)$$

Thus, a smooth transition between the latent space and data space can be achieved by progressively doubling layer widths, eliminating the need for arbitrary choices while maintaining relaxed compliance with KART. Strict adherence to KART can be achieved for hidden layer  $h_{l_k,l_{k-1}}$  by applying either a sigmoid or affine transformation after layer  $h_{l_{k-2},l_{k-3}}$  to shift its range back to  $[0, 1]^{L_{k-1}}$ . However, using sigmoid may lead to vanishing gradients and we suggest that function domains are less critical to KART than its structural properties and should not be prioritized over maintaining gradient flow and avoiding saturation.

Adopting a KAN-based generator also allows for training with L1 regularization, followed by pruning with the method proposed by Liu et al. (2024). This enables further model compression beyond the baseline structure defined by KART.

#### 2.3.2 MIXTURE PRIOR

As noted in Sec. 2.1, the independence of the priors  $\pi_{q,p}$  limits expressivity. Moreover, the summation over  $p$  in Eq. 9 accumulates the variances of sampled  $z_{q,p}$ , which can lead to overly diffuse representations. To address this, particularly for more complex generative tasks such as those in Sec. 3.2, we relax the strict adherence to KART by reformulating the prior as a mixture distribution,

similar to the approach described by Rivera (2024). This involves moving the summation over  $p$  from 1 to  $n_z$  out of the generator and absorbing it into the prior, yielding a mixture density:

$$p_{\mathbf{f},q}(z) = \sum_{p=1}^{n_z} \alpha_{q,p} \frac{\exp(f_{q,p}(z))}{Z_{q,p}} \pi_0(z), \quad \text{where} \quad \sum_{p=1}^{n_z} \alpha_{q,p} = 1, \quad \alpha_{q,p} \geq 0. \quad (13)$$

Here,  $\alpha_{q,p}$  represent the mixture proportions, which must satisfy non-negativity and unit-sum constraints. In this study, they were fixed uniformly as  $1/n_z$ , guided by Rivera (2024). They could alternatively be learned by passing trainable parameters through a softmax function, (to enforce the constraints), however this approach was not used for the experiments in Sec. 3.

The result is a mixture of energy-based priors. Sampling becomes more efficient than in the previous formulation, as it proceeds component-wise using ITS for discrete variables, (Devroye, 2006). However, this violates KART, since  $F$  now corresponds to a discrete rather than continuous CDF.

The mixture proportions are learned by replacing the log-prior in Eq. 18 with the logarithm of Eq. 13. To encourage balanced weighting and reduce model complexity, L1 regularization can be applied to  $\alpha_{q,p}$  and small values can be pruned. Component selection follows a categorical distribution over  $p = 1, \dots, n_z$ , determined by  $\alpha_{q,p}$ . Let  $u_{\text{mix}} \sim \text{Unif}(0, 1)$ . Guided by Devroye (2006) regarding how ITS applied to discrete variables, the selected component  $p^*$  is given by:

$$p^* = \min \left\{ j \mid \sum_{p=1}^j \alpha_{q,p} \geq u_{\text{mix}} \right\}. \quad (14)$$

This ensures that each component  $p^*$  is selected with probability  $\alpha_{q,p^*}$ . ITS can then be used to sample from the chosen component, (see 2.4.3).

## 2.4 MAXIMUM LIKELIHOOD TRAINING

With  $N_x$  training examples in a batch, the optimization objective is the minimization of the negative log-marginal likelihood:

$$\min_{\mathbf{f}, \Phi} \mathcal{L}(\mathbf{x}^{(1)}, \dots, \mathbf{x}^{(N_x)}) = \min_{\mathbf{f}, \Phi} \left[ - \sum_{b=1}^{N_x} \log \left( p_{\mathbf{f}, \Phi}(\mathbf{x}^{(b)}) \right) \right]. \quad (15)$$

The dependency on the collection,  $\mathbf{f}, \Phi$ , represents all learnable elements of KAEM. For each sample of  $\mathbf{x}^{(b)}$ , the log-marginal likelihood in Eq. 15 can be separated out into two log-densities by first introducing the latent vector,  $\mathbf{z}$ , otherwise absent upon marginalization over the latent space. This is shown under Sec. A.4.2, and the resulting expectation exhibits a lack of dependence on sampling, as proven under Sec. A.4.3:

$$\nabla_{\mathbf{f}, \Phi} \left[ \log p_{\mathbf{f}, \Phi}(\mathbf{x}^{(b)}) \right] = \mathbb{E}_{p_{\mathbf{f}, \Phi}(\mathbf{z} | \mathbf{x}^{(b)})} \left[ \nabla_{\mathbf{f}} [\log p_{\mathbf{f}}(\mathbf{z})] + \nabla_{\Phi} \left[ \log p_{\Phi}(\mathbf{x}^{(b)} | \mathbf{z}) \right] \right], \quad (16)$$

### 2.4.1 LOG-PRIOR

Given the independence of the prior’s parameters, the log-prior can be modeled as a sum over the univariate cases:

$$\log \left( p_{\mathbf{f}}(\mathbf{z}) \right) = \sum_{q=1}^{2n_z+1} \sum_{p=1}^{n_z} \log \left( \pi_{q,p}(z_{q,p}) \right) = \sum_{q=1}^{2n_z+1} \sum_{p=1}^{n_z} f_{q,p}(z_{q,p}) + \log \left( \pi_0(z_{q,p}) \right) - \log \left( Z_{q,p} \right) \quad (17)$$

Tractable normalization is available through Eq. 6, however it may be more efficient to discard normalization in the learning gradient. In Sec. A.4.4, we derive the contrastive divergence learning gradient for KAEM, which faster to train and more typical of energy-based modeling:

$$\mathbb{E}_{p_{\mathbf{f}, \Phi}(\mathbf{z} | \mathbf{x})} \left[ \nabla_{\mathbf{f}} [\log p_{\mathbf{f}}(\mathbf{z})] \right] = \mathbb{E}_{p_{\mathbf{f}, \Phi}(\mathbf{z} | \mathbf{x})} \left[ \nabla_{\mathbf{f}} \sum_{q=1}^{2n_z+1} \sum_{p=1}^{n_z} f_{q,p}(z_{q,p}) \right] - \mathbb{E}_{p_{\mathbf{f}}(\mathbf{z})} \left[ \nabla_{\mathbf{f}} \sum_{q=1}^{2n_z+1} \sum_{p=1}^{n_z} f_{q,p}(z_{q,p}) \right]. \quad (18)$$

Here,  $\mathbf{z}$  is sampled from  $p_f(\mathbf{z})$  and  $p_{f,\Phi}(\mathbf{z} \mid \mathbf{x}^{(b)})$  and reflects a univariate element of the prior model. The expectation with respect to the posterior can be approximated using Importance Sampling (IS), outlined under Secs. 2.4.4 & A.5.1, or a standard Monte Carlo estimator when using Langevin sampling methods. The prior expectation may always be approximated with a Monte Carlo estimator taken across samples:

$$\mathbb{E}_{p_f(\mathbf{z})} \left[ \nabla_{\mathbf{f}} \sum_{q=1}^{2n_z+1} \sum_{p=1}^{n_z} f_{q,p}(z_{q,p}) \right] \approx \frac{1}{N_s} \sum_{s=1}^{N_s} \nabla_{\mathbf{f}} \sum_{q=1}^{2n_z+1} \sum_{p=1}^{n_z} f_{q,p}(z_{q,p}^{(s)}) \quad \text{where } z_{q,p}^{(s)} \sim p_{q,p}(\mathbf{z}). \quad (19)$$

The gradient of Eq. 18 can therefore be viewed as a element-wise correction to the prior, incorporating information from the observations to align the prior with the posterior, thereby following the philosophy of empirical Bayes. The gradient can then be evaluated via autodifferentiation.

#### 2.4.2 LOG-LIKELIHOOD

Depending on the task the log-likelihood can be modeled in multiple ways. For example, a Gaussian model might be adopted for images, and an autoregressive model for text. It can also be realized into a multimodal generative modeling framework using the principles outlined by Yuan et al. (2024).

$$\log \left( p_{\Phi} \left( \mathbf{x}^{(b)} \mid \mathbf{z} \right) \right) = \begin{cases} -\frac{\|\mathbf{x}^{(b)} - \tilde{\mathbf{x}}\|_2^2}{2\sigma_{\text{llhood}}^2} + \text{const}, & \text{(static continuous data)} \\ \sum_{o=1}^{n_x} \sum_{c=1}^K x_{o,c}^{(b)} \log \tilde{x}_{o,c} + \text{const}, & \text{(static discrete data)} \\ \sum_{t=1}^T \log \left( p_{\Phi} \left( \mathbf{x}^{(b,t)} \mid \mathbf{x}^{(b,1)}, \dots, \mathbf{x}^{(b,t-1)}, \mathbf{z} \right) \right), & \text{(sequential data)} \end{cases} \quad (20)$$

Here,  $\tilde{\mathbf{x}}$  is a generated sample from Eq. 9 corresponding to a single batch item,  $\mathbf{x}^{(b)}$ ,  $\sigma_{\text{llhood}}$  is a hyperparameter subject to assumptions regarding the variance of the data, and  $K$  denotes the number of discrete classes. The learning gradient attributed to the log-likelihood can also be evaluated using autodifferentiation, after first approximating the posterior expectation with IS or MC estimators.

The code in Sec. A.1 also provides an option to augment the first likelihood model with an additional perceptual loss term (Johnson et al., 2016) using features extracted from the pretrained VGG-16 CNN (Simonyan & Zisserman, 2015). This could have yielded higher-fidelity images for Sec. 3.2, but it was not adopted in this study due to the computational overhead of Langevin sampling.

#### 2.4.3 PRIOR INVERSE TRANSFORM SAMPLING

In Eqs. 9 & 19,  $z_{q,p}$  is drawn from  $p_{q,p}$  with inverse transform sampling, (ITS) (Devroye, 1986). ITS can be used to sample from a component of the latent density,  $p_{q,p}$ , made possible given the unique characteristics of KAEM. Specifically, the univariate, finite-grid structure of the KAN-based energy functions enables quadrature/interpolating integral approximations.

1. **CDF inversion:** Sampling occurs using the inverse cumulative density function (CDF): The CDF for a single component,  $F_{\pi_{q,p}}$ , is:

$$F_{\pi_{q,p}}(z') = \frac{\int_{z_{\min}}^{z'} \exp(f_{q,p}(z)) \pi_0(z) dz}{Z_{q,p}}, \quad Z_{q,p} = \int_{z_{\min}}^{z_{\max}} \exp(f_{q,p}(z)) \pi_0(z) dz. \quad (21)$$

These two integrals can be conveniently and efficiently approximated using Gauss-Kronrod quadrature, (Laurie, 1997), given that  $f_{q,p}$  is univariate and defined on a bounded grid:

$$G(z) = \exp(f_{q,p}(z)) \pi_0(z), \quad \int_{z_{\min}}^{z'} G(z) dz \approx \sum_{i=1}^{N_{\text{quad}}} w_i G(z_i^{\text{node}}), \quad (22)$$

where  $z_i^{\text{node}}$  and  $w_i$  are the Gauss-Legendre quadrature nodes and weights for the interval  $[z_{\min}, z']$ . A random variable is uniformly drawn and shared across  $q$ ,  $u_p \sim \text{Unif}(0, 1)$ . The

first interval where  $F_{\pi_{q,p}}(z)$  is greater than  $u_p$  scaled by  $Z_{q,p}$  is identified:

$$k^* = \min \left\{ j \mid \sum_{i=1}^j w_i G(z_i^{\text{node}}) \geq Z_{q,p} \cdot u_p \right\}. \quad (23)$$

2. **Linear interpolation:** The sample  $z_p$  is interpolated within the subset,  $[z_{k^*-1}^{\text{node}}, z_{k^*}^{\text{node}}]$ :

$$z_p \approx z_{k^*-1}^{\text{node}} + (z_{k^*}^{\text{node}} - z_{k^*-1}^{\text{node}}) \cdot \frac{u_p - F_{\pi_{q,p}}(z_{k^*-1}^{\text{node}})}{F_{\pi_{q,p}}(z_{k^*}^{\text{node}}) - F_{\pi_{q,p}}(z_{k^*-1}^{\text{node}})}. \quad (24)$$

The procedure ensures an efficient, exact and unbiased generation of samples,  $z_{q,p}$ , distributed according to  $p_{q,p}$ . It can be vectorized to generate samples from all prior elements.

#### 2.4.4 POSTERIOR EXPECTATIONS WITH IMPORTANCE SAMPLING

The log-marginal likelihood and its learning gradient presented in Eqs. 15 & 16, involve expectations with respect to the posterior  $p_{f,\Phi}(z \mid \mathbf{x}^{(b)})$ , which is potentially multimodal and complex. We propose Importance Sampling (IS) (Goertzel, 1949) as an efficient method for estimating its expectation when datasets are simple or when task knowledge can be incorporated into the model to improve prior-posterior alignment and the quality of the IS estimator.

IS provides a quick approximation of the posterior expectation without requiring extensive exploration. In contrast, ULA, (introduced in Sec. 2.5.2) is more stochastic and exploratory, often yielding higher-quality samples from the posterior, when the prior is poorly matched.

The following procedure is elaborated in more detail under Sec. A.5.1:

1. **Proposal distribution:**  $N_s$  independent samples,  $\{\mathbf{z}^{(s)}\}_{s=1}^{N_s}$ , are drawn from the proposal,  $q(\mathbf{z}) = p_f(\mathbf{z})$ , which the target,  $p_{f,\Phi}(z \mid \mathbf{x}^{(b)})$  must be absolutely continuous with respect to. Sampling from the prior is tractable with the procedure outlined in Sec. 2.4.3.
2. **Importance weights:** The normalized importance weights are evaluated:

$$w_{\text{norm}}(\mathbf{z}^{(s)}) = \frac{w(\mathbf{z}^{(s)})}{\sum_{r=1}^{N_s} w(\mathbf{z}^{(r)})} = \text{softmax}_s \left( \log(p_{\Phi}(\mathbf{x}^{(b)} \mid \mathbf{z}^{(s)})) \right). \quad (25)$$

3. **Effective Sample Size:** To prevent weight degeneracy, resampling is conducted when the Effective Sample Size (ESS) falls below a threshold specified by a hyperparameter,  $\gamma$ :

$$ESS = \frac{1}{\sum_{s=1}^{N_s} w_{\text{norm}}(\mathbf{z}^{(s)})} < \gamma \cdot N_s. \quad (26)$$

Otherwise, the weights are taken without alteration, (i.e. the next step is skipped). When the weights are uniformly spread the ESS evaluates to  $N_s$ . High-variance weights with a low ESS indicate that many samples contribute minimally, resulting in inefficient sampling. Resampling focuses learning on samples that are more representative of the posterior distribution, which maximizes the usefulness of each parameter update.

4. **Resample:** If required, the population,  $\{\mathbf{z}^{(s)}, w_{\text{norm}}(\mathbf{z}^{(s)})\}_{s=1}^{N_s}$ , is resampled from. There are multiple ways to accomplish this, (Douc et al., 2005). Systematic, stratified, and residual resampling are provided in the codebase under Sec. A.1, parallelized across samples. In this study, we adopted residual resampling, (explained under Sec. A.5.2).
5. **Expectation estimation:** After resampling, IS weights are uniformly distributed and the posterior expectation of an arbitrary function or density,  $\rho(\mathbf{z})$ , (e.g., the log-likelihood), is estimated with a Monte Carlo estimator:

$$\mathbb{E}_{p_{f,\Phi}(z|\mathbf{x}^{(b)})}[\rho(\mathbf{z})] \approx \sum_{s=1}^{N_s} \rho(\mathbf{z}^{(s)}) \cdot w_{\text{norm}}(\mathbf{z}^{(s)}) \approx \frac{1}{N_s} \sum_{s=1}^{N_s} \rho(\mathbf{z}_{\text{resampled}}^{(s)}). \quad (27)$$

This is used to estimate the log-marginal likelihood and its gradient in Eqs. 15 and 16. However, unlike ULA (discussed in Sec. 2.5.2 and demonstrated in Sec. 3.2), IS fails to support posterior exploration when the prior is poorly aligned, making it unsuitable for general-purpose tasks beyond those similar to the datasets presented in Secs. 3.1.

## 2.5 POPULATION-BASED AND LANGEVIN MONTE CARLO POSTERIOR SAMPLING

To mitigate the poor convergence of multimodal ULA sampling, we introduce a training criterion that facilitates posterior annealing. Details on the cyclic annealing schedule adopted in this study, along with practical guidance on hyperparameter selection, are provided in Sec. A.3.

### 2.5.1 THERMODYNAMIC TRAINING CRITERION

We inform our derivations using the Thermodynamic Integral. In place of the log-marginal likelihood outlined in Eq. 15, this uses the following representation derived in Sec. A.4.5:

$$\log \left( p_{f, \Phi}(\mathbf{x}^{(b)}) \right) = \int_0^1 \mathbb{E}_{p_{f, \Phi}(\mathbf{z} | \mathbf{x}^{(b)}, t)} \left[ \log \left( p_{\Phi}(\mathbf{x}^{(b)} | \mathbf{z}) \right) \right] dt \quad (28)$$

Here,  $p_{f, \Phi}(\mathbf{z} | \mathbf{x}^{(b)}, t)$  has been introduced as the power posterior, which can be considered a representation of the original posterior, with a likelihood tempered by a temperature parameter,  $t$ . This is introduced by Friel & Pettitt (2008) and organized for our purposes as follows:

$$p_{f, \Phi}(\mathbf{z} | \mathbf{x}^{(b)}, t) = \frac{p_{\Phi}(\mathbf{x}^{(b)} | \mathbf{z})^t \cdot p_f(\mathbf{z})}{Z_t},$$

$$\text{where } Z_t = \mathbb{E}_{p_f(\mathbf{z})} \left[ p_{\Phi}(\mathbf{x}^{(b)} | \mathbf{z})^t \right] = \int_{\mathcal{Z}} p_{\Phi}(\mathbf{x}^{(b)} | \mathbf{z})^t \mathbb{P}_f(d\mathbf{z}) \quad (29)$$

Given the form of Eq. 29, setting  $t = 0$  results in the power posterior density assuming the form of the prior. As  $t$  increments, the power posterior gradually adopts a shape more closely resembling the true Bayesian posterior. At  $t = 1$ , the power posterior converges fully on the original posterior.

The effect of tempering is illustrated in Fig. 1, starting with a Gaussian prior that is entirely un-informed of  $\mathbf{x}^{(b)}$ . As  $t$  increases from 0 to 1, the contribution of the likelihood term in Eq. 29 progressively grows, ultimately leading to the posterior at  $t = 1$ . This final posterior can be interpreted as the prior updated by information from the samples of  $\mathbf{x}^{(b)}$ .

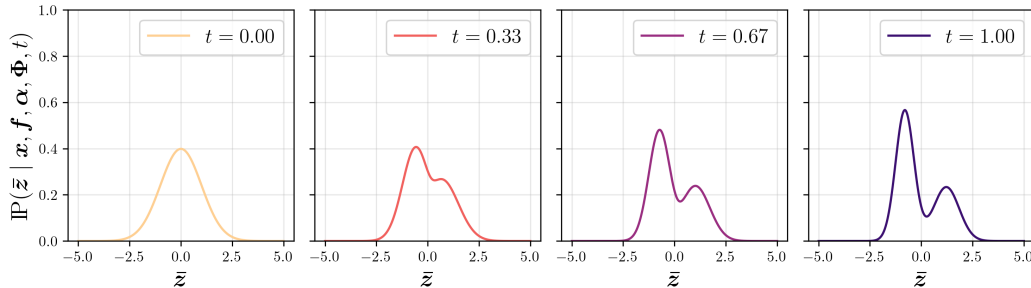


Figure 1: Demonstration of power posterior evolution with  $t$ . A simple Gaussian prior is sculpted into forms that resemble a more complex, multi-modal posterior as  $t$  is incremented from 0 to 1.

The exact calculation of the integral in Eq. 28 is feasible given that the bounds are  $t = 0$ , corresponding to the expectation being taken with respect to the prior, and  $t = 1$ , where it is taken with respect to the posterior. However, the integral can also be expressed exactly without collapsing the temperatures. This allows greater flexibility in how the integral evolves through the temperature schedule,  $\{t_k\}_{k=0}^{N_t}$ . In particular, the temperature schedule is discretized as:

$$\mathbf{t} = (t_0, t_1, \dots, t_{N_t}), \quad t_k \in [0, 1] \quad (30)$$

In Sec. A.4.7, the Steppingstone estimator (SE) introduced by Annis et al. (2019) is derived from the discretized Thermodynamic Integral presented by Calderhead & Girolami (2009), (and provided under Sec. A.4.6). This establishes a connection between the two, which we use to derive the

learning gradient and inform our approach to the clustering the temperatures in Eq. 30:

$$\log \left( p_{\mathbf{f}, \Phi}(\mathbf{x}^{(b)}) \right) = \sum_{k=1}^{N_t} \log \left( \frac{\mathbf{Z}_{t_k}}{\mathbf{Z}_{t_{k-1}}} \right) = \sum_{k=1}^{N_t} \left( \log(\mathbf{Z}_{t_k}) - \log(\mathbf{Z}_{t_{k-1}}) \right) = \underbrace{\log(\mathbf{Z}_{t_{N_t}})}_{=\text{MLE}} - \underbrace{\log(\mathbf{Z}_{t_0})}_{=0 \text{ (Eq. 36)}}. \quad (31)$$

The log-partition ratios are estimated with Monte Carlo estimators using all annealed samples:

$$\begin{aligned} \log \left( p_{\mathbf{f}, \Phi}(\mathbf{x}^{(b)}) \right) &= \log(\mathbf{Z}_{t_{N_t}})^{\text{SS}} = \sum_{k=1}^{N_t} \log \left( \frac{\mathbf{Z}_{t_k}}{\mathbf{Z}_{t_{k-1}}} \right) \\ &\approx \frac{1}{N_s} \sum_{k=1}^{N_t-1} \sum_{s=1}^{N_s} (t_{k+1} - t_k) \left[ \log p_{\Phi} \left( \mathbf{x}^{(b)} \mid \mathbf{z}^{(s, t_k)} \right) \right], \quad \text{where } \underbrace{\mathbf{z}^{(s, t_k)} \sim p_{\mathbf{f}, \Phi}(\mathbf{z} \mid \mathbf{x}^{(b)}, t_k)}_{\text{Sec. 2.5.2}} \end{aligned} \quad (32)$$

SE and its variants, such as Annealed Importance Sampling (AIS) (Neal, 1998), are commonly used to estimate a model’s evidence without a tractable way to learn the prior, as they lack dependence on prior gradients beyond sampling. However, by recognizing the direct connection between the SE and MLE learning gradients, as proven in Sec. A.4.7, one can simply add the contrastive divergence learning gradient from Eq. 18 to the SE estimator.

This is valid because the SE gradient matches the MLE gradient, and the likelihood gradient is independent of the prior gradient. The posterior expectation of contrastive divergence in Eq. 18 can be estimated with a Monte Carlo estimator using the final samples of ULA.

## 2.5.2 UNADJUSTED LANGEVIN ALGORITHM (ULA) AND REPLICA EXCHANGE

In their implementation of Thermodynamic Integration, Calderhead & Girolami (2009) estimated the Thermodynamic Integral using the discretization in Sec. A.4.6, using population-based MCMC and Parallel Tempering (PT) (Swendsen & Wang, 1986; Marinari & Parisi, 1992; Hukushima & Nemoto, 1996) to simultaneously sample from all power posteriors.

Specifically, parallel chains were maintained at each temperature, (or Replica), using Metropolis-Hastings (MH) (Metropolis & Ulam, 1949), to drive local moves for each power posterior. They also proposed a geometric path between the prior and posterior, enabling global swaps between adjacent temperatures. This approach allowed higher temperatures to leverage the efficient mixing of lower temperatures, thereby facilitating a more thorough exploration of the posterior landscape.

We adopt a similar strategy but follow Pang et al. (2020) in using the Unadjusted Langevin Algorithm (ULA) (Rosicky et al., 1978b; Brooks et al., 2011) without MH correction. Specifically, we update samples using the forward Euler-Maruyama discretization of the Langevin SDE, as detailed by Roberts & Stramer (2002):

$$\mathbf{z}^{(i+1, t_k)} = \mathbf{z}^{(i, t_k)} + \eta \nabla_{\mathbf{z}^{(i, t_k)}} \log \gamma \left( \mathbf{z}^{(i, t_k)} \right) + \sqrt{2\eta} \boldsymbol{\epsilon}^{(i, t_k)}, \quad (33)$$

where  $\eta$  is the step size,  $\boldsymbol{\epsilon}^{(i, t_k)} \sim \mathcal{N}(\mathbf{0}, \mathbf{I})$ , and  $\gamma_{t_k}$  denotes the target power posterior:

$$\log \gamma \left( \mathbf{z}^{(i, t_k)} \right) = \log p_{\mathbf{f}, \Phi}(\mathbf{z}^{(i, t_k)} \mid \mathbf{x}^{(b)}, t_k) \propto t_k \log p_{\Phi}(\mathbf{x}^{(b)} \mid \mathbf{z}^{(i, t_k)}) + \log p_{\mathbf{f}}(\mathbf{z}^{(i, t_k)}).$$

ULA is best suited for smooth, unimodal distributions, but annealing with power posteriors can improve sampling from multimodal distributions. Mixing can be further improved by periodically swapping populations between randomly selected adjacent temperatures, subject to:

$$r = \frac{p_{\Phi}(\mathbf{x}^{(b)} \mid \mathbf{z}^{(i, t_{k+1})})^{t_k} p_{\Phi}(\mathbf{x}^{(b)} \mid \mathbf{z}^{(i, t_k)})^{t_{k+1}}}{p_{\Phi}(\mathbf{x}^{(b)} \mid \mathbf{z}^{(i, t_k)})^{t_k} p_{\Phi}(\mathbf{x}^{(b)} \mid \mathbf{z}^{(i, t_{k+1})})^{t_{k+1}}}, \quad (34)$$

where the proposed swap,  $\mathbf{z}^{(i, t_{k+1})} \leftrightarrow \mathbf{z}^{(i, t_k)}$ , is accepted with probability:  $\min(1, r)$ .

### 3 EXPERIMENTS

Our experiments are designed to highlight the unique advantages of our contributions and compare the proposed strategies for scaling and training KAEM. Radial basis functions (RBFs) (Li, 2024) were used as the univariate functions in place of the cubic B-spline interpolations proposed by Liu et al. (2024). Benchmarks are provided in Sec. A.2.

In Sec. 3.1, we show that importance sampling becomes a viable and highly efficient training strategy for simple datasets, due to the low dimensionality of the latent space. We also demonstrate that the model remains effective when strictly adhering to KART with independent energy-based priors, thereby validating the use of KART as a source of structural inductive bias.

In Sec. 3.2, we evaluate the mixture EBM prior, sampled via component-wise ITS and paired with CNN-decoder architectures, which are slightly smaller variants of those used by Pang et al. (2020). We additionally compare KAEM trained using single-posterior ULA sampling with the MLE criterion against a population-based ULA sampling strategy using the SE criterion. These comparisons assess the practicality of using mixture densities for scaling KAEM and using annealing to improve training for high-dimensional RGB images.

To quantify the fidelity of generated data in a more reliable manner than previous studies in the literature, we used effectively unbiased metrics based on the principles outlined by Chong & Forsyth (2020). By applying linear regression to extrapolate the values of standard metrics to an infinitely sized sample set, Monte Carlo error was mitigated, (otherwise associated with finite sample sizes).

For Sec. 3.2, we gathered  $\overline{\text{FID}}_\infty$  and  $\overline{\text{KID}}_\infty$ , which are effectively unbiased estimators of the Fréchet Inception Distance and Kernel Inception Distance, introduced by Heusel et al. (2018); Bińkowski et al. (2021) respectively. The set of sample sizes used for the linear regression were: 1000, 1200, 1400, 1600, 1800, 2000, 2200, 2400, 2600, 2800, 3000.

However, we recognise that quantifying the fidelity of generated data is inherently challenging and not an exact science. While the metrics used in this study have limitations, they align with those commonly found in the literature. Our conclusions are also informed by our subjective perception of the images. Furthermore, no metrics were applied in Secs. 3.1.1 & 3.1.1, as vision metrics rely on the Inception V3 model trained on ImageNet (Szegedy et al., 2015), potentially introducing bias against other datasets, especially non-RGB images.

#### 3.1 IMPORTANCE SAMPLING

##### 3.1.1 MNIST & FMNIST

The MNIST (Deng, 2012) and FMNIST (Xiao et al., 2017) datasets are grayscale datasets that can be modeled with the first likelihood model from Eq. 20. The first collection of benchmarks presented in Sec. A.2 were obtained using the hyperparameters and architecture specified for this experiment in Tab. 4. KAEM was trained for 10 epochs with 50,000 training examples, an importance sample size of  $N_s = 100$ , and a batch size of  $N_x = 100$ , (corresponding to 5,000 parameter updates). Prior sampling was conducted with ITS and posterior expectations were estimated with IS. The architecture was guided by KART and independent priors were used.

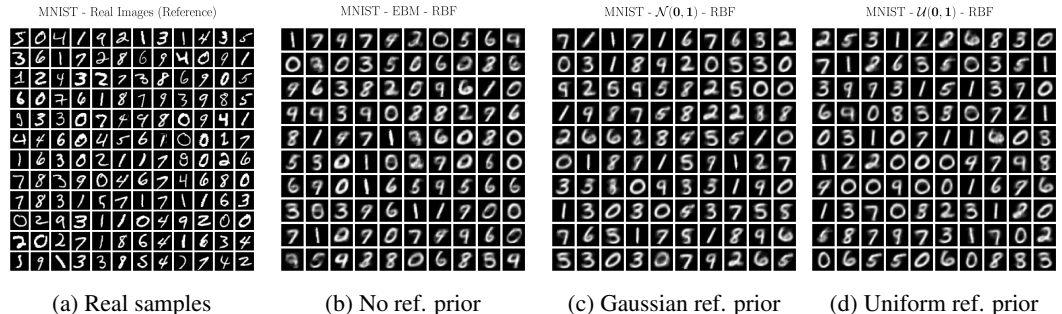


Figure 2: Generated MNIST examples using different reference priors

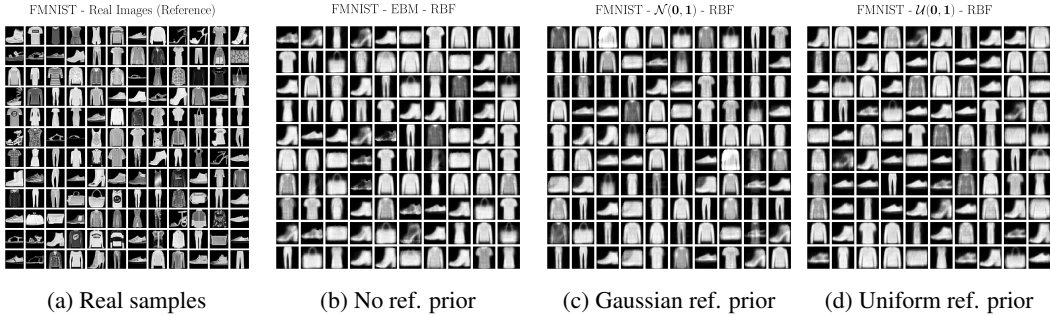


Figure 3: Generated FMNIST examples using different reference priors

KAEM consistently generated a diverse set of samples when non-restrictive reference priors were used, (Gaussian, uniform, or no reference), thus validating importance sampling, independent energy-based priors, and strict adherence to KART for simple datasets.

Fig. 4 depicts a single latent component of KAEM trained on FMNIST with a Gaussian reference prior, demonstrating KAEM’s potential for latent prior discovery.

Generally, priors were modified minimally when trained with IS, and remained largely aligned with their reference distributions. This suggests that the reference prior used to initialize KAEM guides the structure of the resulting latent space and may provide a useful source of inductive bias or reusable structure.

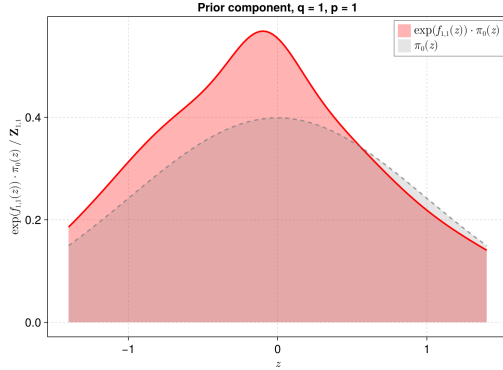


Figure 4: Component  $p_{q=1,p=1}(z)$  after training on FMNIST. The density has been normalized by  $Z_{q=1,p=1}$  using quadrature, however there is a small discretization bias preventing exactness.

### 3.2 LANGEVIN MONTE CARLO AND STEPPINGSTONE ESTIMATOR

KAEM, when adherent to KART, can be interpreted as a dense or spline-based network. However, for spatial data, convolutional neural networks (CNNs) (LeCun et al., 2015), are more suitable as the generator,  $\mathcal{G}$ . In addition to their computational efficiency through weight sharing, CNNs offer a key advantage over dense networks due to their spatial inductive bias: sequences of convolutional layers implement shift-equivariant transformations that are well-suited for images.

We evaluated KAEM using a CNN generator against two RGB image datasets at different resolutions, SVHN ( $32 \times 32$ ) (Netzer et al., 2011) and CelebA ( $64 \times 64$ ) (Liu et al., 2015). The first likelihood model in Eq. 20 was adopted for both datasets. Due to limited computational resources during this study, (detailed in Sec. A.2), training was shortened to 16,000 parameter updates, (70,000 were used in the study by Pang et al. (2020)), and the CNN decoder architectures used by Pang et al. (2020) were adopted as the generators.

A single optimizer (Adam) was used to train both models, rather than using separate optimizers for the prior and generator. Full architectural details are provided under Sec. A.6.1. Posterior sampling was conducted with 40 steps of ULA, and a standard Gaussian reference prior was used,  $\pi_0 = \mathcal{N}(0, 1)$ . KAEM was trained for 40 epochs with a batch size of  $N_x = 50$  on 20,000 training examples. All remaining hyperparameters are in Tab. 5. Annealing was conducted with  $N_t = 5$  power posteriors and the  $p$  scheduling outlined in Sec. A.3.1.

Table 1: Effectively unbiased FID and KID scores (lower is better) for SVHN ( $32 \times 32$ ).

MLE	SE
$\overline{\text{FID}}_\infty = 78.41$	$\overline{\text{FID}}_\infty = 165.79$
$\overline{\text{KID}}_\infty = 0.0627$	$\overline{\text{KID}}_\infty = 0.1608$

Table 2: Effectively unbiased FID and KID scores (lower is better) for CelebA ( $64 \times 64$ ).

MLE	SE
$\overline{\text{FID}}_\infty = 130.05$	$\overline{\text{FID}}_\infty = 150.25$
$\overline{\text{KID}}_\infty = 0.1427$	$\overline{\text{KID}}_\infty = 0.1637$

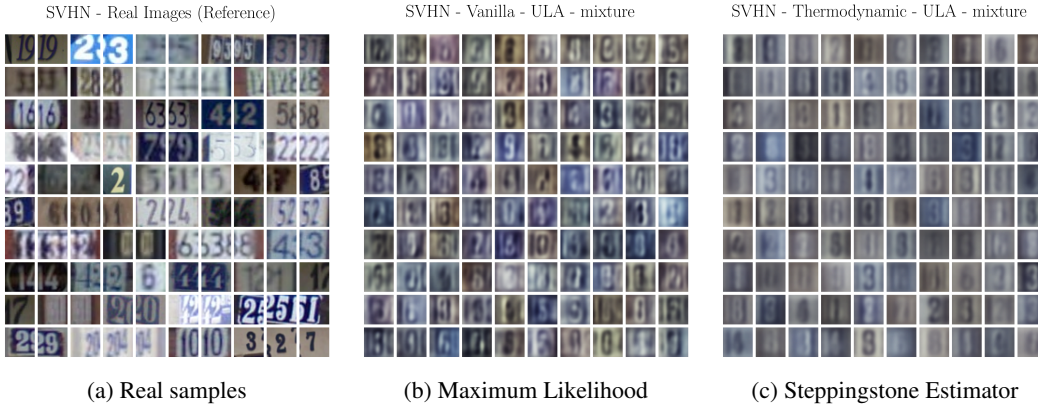


Figure 5: Generated SVHN ( $32 \times 32$ ) examples using mixture prior architecture with inverse transform sampling from the prior and Langevin sampling from the posterior



Figure 6: Generated CelebA ( $64 \times 64$ ) examples using mixture prior architecture with inverse transform sampling from the prior and Langevin sampling from the posterior

Despite being trained with reduced complexity for a small iteration count, our mixture prior model was able to generate low quality samples of SVHN and CelebA. This demonstrates the potential of component-wise ITS for exact and highly efficient sampling in replacement to the approach of Pang et al. (2020), which relied on ULA to sample from the prior, thus introducing bias and inefficiency.

Our proposed SE training strategy resulted in worse image metrics for both datasets. However, from our subjective perspective, the generated CelebA images appeared more well-defined, yet less diverse under SE than under MLE. Future work could investigate when SE might be preferred over MLE, as SVHN performed well under the MLE criterion, whereas CelebA subjectively benefited from SE to produce human-perceptible features. For example, a more optimally tuned annealing schedule might have sharpened SVHN features in a manner similar to its effect on CelebA.

Ultimately, we cannot justify the Thermodynamic training strategy due to its substantial computational overhead. With more VRAM than available in this study, it would be possible to parallelize a

greater number of temperatures than  $N_t = 5$ , which could potentially improve quality, as suggested by the results of Calderhead & Girolami (2009).

More posterior sampling options, such as modified annealing schedules, a larger number of ULA steps, or the use of autoMALA with bias correction and temperature-adaptive step size tuning may further improve results. Nevertheless, exploring these options might not be worthwhile until the hardware described by Zetta (2024) becomes available, given the added algorithmic complexity, hyperparameter sensitivity, and extended training times involved. A better approach to posterior sampling might involve amortized inference similar to Kingma & Welling (2022).

## 4 CONCLUSIONS

KAEM provides a principled, scalable framework for structured and informed generative modeling. Our results demonstrate that importance sampling can enable more efficient training on simple or low-dimensional datasets. We also show how the Kolmogorov-Arnold representation theorem can inform architectural design and introduce structural bias, allowing KAEM’s architecture to be guided entirely by the size of its latent space. Moreover, we find that the inverse transform method offers advantages over Langevin Monte Carlo sampling for energy-based priors in terms of speed and exact sampling. However, the benefits of annealing and population-based MCMC remain inconclusive, suggesting directions for further work. Future investigations into the practicality of our annealing methods depend on continued hardware advancements, such as those introduced by Zetta (2024).

### 4.1 FUTURE WORK

#### 4.1.1 HARDWARE ACCELERATION

Benchmarks are provided in Sec. A.2, compiled to MLIR/XLA using Reactant (EnzymeAD & Reactant.jl Contributors, 2025) and EnzymeMLIR for automatic differentiation (Moses & Churavy, 2020; Moses et al., 2021; 2022).

The univariate, localized nature of B-spline interpolations complicates their parallelization on GPUs, since they involve sparse and recursive computations, so RBF bases were used in replacement. The search operations in Eqs. 14, 23, and 71 are also difficult to parallelize with GPU kernels, since GPUs are generally ill-suited for search algorithms, as they often rely on conditional logic. Parallelizing conditionals can lead to thread divergence, making GPUs inefficient for these operations. To compile the model with Reactant, these algorithms were instead written using sparse multiplications for conditional masking, which was efficient but suboptimal on GPUs.

Additionally, while ITS enables fast inference and scales when the prior is a mixture model, KAEM’s training with ULA does not scale efficiently on GPUs due to the iterative, gradient-based nature of ULA. GPUs are not well suited to Langevin Monte Carlo methods due to the irregular memory access patterns and bandwidth pressure caused by differentiating with respect to inputs, which requires storing the outputs of each layer within the generator.

Nonetheless, the unique advantages of KAEM justify continued research and development. Moreover, Zetta (2024) introduces the Learnable Function Unit (LFU), a processor designed for efficient evaluation and differentiation of univariate, nonlinear functions in parallel, while offering precise data flow control that can mitigate the challenges of sparsity, recursion, and irregular memory access patterns. The LFU presents a promising avenue for more efficient implementations of ULA, and improved posterior sampling, potentially including bias correction and adaptive step size tuning with autoMALA (Biron-Lattes et al., 2024) to assist when a single step size is insufficient for all power posterior geometries. Even without annealing, replacing ULA with autoMALA may yield a more robust probabilistic model with stronger theoretical guarantees.

KAEM might prove more scalable than conventional generative models, owing to its reliance on finite representations of continuous functions and its compatibility with the LFU.

#### 4.1.2 MORE OPPORTUNITIES FOR IMPORTANCE SAMPLING

For SVHN and CelebA, IS proved infeasible as a posterior sampler, so ULA was used for Sec. 3.2. IS is limited by estimator variance, whereas ULA is often limited by mixing and when sampling multimodal distributions, (addressed in this study with annealing).

Therefore, the failure of IS for the more complex datasets might be attributed to prior-posterior mismatch, which rendered the IS estimator ineffective. Moreover, relying on IS restricts the prior to its initial domain, since proposals are generated from the prior using ITS and finite-domain KAN energy functions. In contrast, ULA can explore values of  $z$  beyond this domain, enabling adaptation of the prior domain within the grid-updating scheme for KANs proposed by Liu et al. (2024).

A possible remedy for the curse of dimensionality is to learn in a reduced-order space using Principal Component Analysis (PCA) (Jolliffe & Cadima, 2016), similar to the approach of Kingma et al. (2014), who also applied PCA to train VAEs. To address prior-posterior mismatch, future work might explore how existing domain knowledge can be incorporated to shape the prior’s energy functions and align them with the posterior before training begins. Additionally, efforts should be directed toward selecting appropriate initial domains or adapting the domains dynamically.

Additionally, KAEM could be used to learn domain-specific priors that transfer across generator architectures. In this setting, IS may serve as an efficient strategy for rapidly retraining a new generator on a prior that is already aligned with the posterior before retraining.

#### 4.1.3 EXPRESSIVITY

The requirements for ITS outlined in Sec. 2.1 are quite restrictive, which may limit expressivity at scale. Additionally, it is often desirable to enrich the latent space with more expressive distributions. For example, Normalizing Flows (Papamakarios et al., 2021) achieve this by applying a sequence of reversible transformations that progressively map a simple base distribution into a complex one.

This might be achievable in KAEM by introducing more latent distributions, or revising Eq. 13 into a Mixture of Experts framework (Cai et al., 2024) where  $\alpha_{q,p}$  could be realized as a more flexible kernel to enable different inductive biases. However, this might be expensive for the model by Pang et al. (2020) since its use of Langevin sampling is computationally intense. For example, the previous work of Cui & Han (2024), which divides their latent EBM space using the diffusion strategy by Ho et al. (2020), states that sampling is expensive due to their use of MCMC methods.

KAEM could potentially circumvent the additional cost by using IS as a fast sampler, though this would require addressing its current limitations.

## REFERENCES

- Jeffrey Annis, Nathan J. Evans, Brent J. Miller, and Thomas J. Palmeri. Thermodynamic integration and steppingstone sampling methods for estimating bayes factors: A tutorial. *Journal of Mathematical Psychology*, 89:67–86, April 2019. doi: 10.1016/j.jmp.2019.01.005. URL <https://osf.io/jpnb4>. Epub 2019 Feb 13.
- Leonard Bereska and Efstratios Gavves. Mechanistic interpretability for ai safety – a review, 2024. URL <https://arxiv.org/abs/2404.14082>.
- Mikołaj Bińkowski, Danica J. Sutherland, Michael Arbel, and Arthur Gretton. Demystifying mmd gans, 2021.
- Miguel Biron-Lattes, Nikola Surjanovic, Saifuddin Syed, Trevor Campbell, and Alexandre Bouchard-Côté. automala: Locally adaptive metropolis-adjusted langevin algorithm, 2024. URL <https://arxiv.org/abs/2310.16782>.
- Pakshal Bohra, Joaquim Campos, Harshit Gupta, Shayan Aziznejad, and Michael Unser. Learning activation functions in deep (spline) neural networks. *IEEE Open Journal of Signal Processing*, 1:295–309, 2020. doi: 10.1109/OJSP.2020.3039379.
- Steve Brooks, Andrew Gelman, Galin Jones, and Xiao-Li Meng. *Handbook of Markov Chain Monte Carlo*. Chapman and Hall/CRC, May 2011. ISBN 9780429138508. doi: 10.1201/b10905. URL <http://dx.doi.org/10.1201/b10905>.

- Weilin Cai, Juyong Jiang, Fan Wang, Jing Tang, Sunghun Kim, and Jiayi Huang. A survey on mixture of experts, 2024. URL <https://arxiv.org/abs/2407.06204>.
- Ben Calderhead and Mark Girolami. Estimating bayes factors via thermodynamic integration and population mcmc. *Computational Statistics & Data Analysis*, 53(12):4028–4045, 2009. ISSN 0167-9473. doi: <https://doi.org/10.1016/j.csda.2009.07.025>. URL <https://www.sciencedirect.com/science/article/pii/S0167947309002722>.
- Min Jin Chong and David Forsyth. Effectively unbiased fid and inception score and where to find them, 2020.
- Jiali Cui and Tian Han. Learning latent space hierarchical ebm diffusion models, 2024. URL <https://arxiv.org/abs/2405.13910>.
- Li Deng. The mnist database of handwritten digit images for machine learning research. *IEEE Signal Processing Magazine*, 29(6):141–142, 2012.
- Luc Devroye. *Non-Uniform Random Variate Generation*. Springer-Verlag, New York, 1986. ISBN 0-387-96305-7.
- Luc Devroye. Chapter 4 nonuniform random variate generation. In Shane G. Henderson and Barry L. Nelson (eds.), *Simulation*, volume 13 of *Handbooks in Operations Research and Management Science*, pp. 83–121. Elsevier, 2006. doi: [https://doi.org/10.1016/S0927-0507\(06\)13004-2](https://doi.org/10.1016/S0927-0507(06)13004-2). URL <https://www.sciencedirect.com/science/article/pii/S0927050706130042>.
- Randal Douc, Olivier Cappé, and Eric Moulines. Comparison of resampling schemes for particle filtering, 2005. URL <https://arxiv.org/abs/cs/0507025>.
- Paul Dupuis and Hui Wang. Importance sampling, large deviations, and differential games. *Stochastics and Stochastic Reports*, 76:481–508, 2004.
- S. Dzhenezher and A. Skopenkov. A structured proof of kolmogorov’s superposition theorem, 2022. URL <https://arxiv.org/abs/2105.00408>.
- EnzymeAD and Reactant.jl Contributors. Reactant.jl: Optimize julia functions with mlir and xla. <https://github.com/EnzymeAD/Reactant.jl>, 2025. Julia package. Version v0.2.181, accessed 2025-12-07.
- N. Friel and A. N. Pettitt. Marginal likelihood estimation via power posteriors. *Journal of the Royal Statistical Society. Series B (Statistical Methodology)*, 70(3):589–607, 2008. ISSN 13697412, 14679868. URL <http://www.jstor.org/stable/20203843>.
- Hao Fu, Chunyuan Li, Xiaodong Liu, Jianfeng Gao, Asli Celikyilmaz, and Lawrence Carin. Cyclical annealing schedule: A simple approach to mitigating kl vanishing, 2019. URL <https://arxiv.org/abs/1903.10145>.
- Alexander B. Givental, Boris A. Khesin, Jerrold E. Marsden, Alexander N. Varchenko, Victor A. Vassiliev, Oleg Ya. Viro, and Vladimir M. Zakalyukin (eds.). *On the representation of functions of several variables as a superposition of functions of a smaller number of variables*, pp. 25–46. Springer Berlin Heidelberg, Berlin, Heidelberg, 2009. ISBN 978-3-642-01742-1. doi: 10.1007/978-3-642-01742-1\_5. URL [https://doi.org/10.1007/978-3-642-01742-1\\_5](https://doi.org/10.1007/978-3-642-01742-1_5).
- Gerald Goertzel. Quota sampling and importance functions in stochastic solution of particle problems. Technical Report AECD-2793, U.S. Atomic Energy Commission, 1949. Technical Report, June 21, 1949.
- Ian J. Goodfellow, Jean Pouget-Abadie, Mehdi Mirza, Bing Xu, David Warde-Farley, Sherjil Ozair, Aaron Courville, and Yoshua Bengio. Generative adversarial networks, 2014. URL <https://arxiv.org/abs/1406.2661>.
- Martin Heusel, Hubert Ramsauer, Thomas Unterthiner, Bernhard Nessler, and Sepp Hochreiter. Gans trained by a two time-scale update rule converge to a local nash equilibrium, 2018.

- Jonathan Ho, Ajay Jain, and Pieter Abbeel. Denoising diffusion probabilistic models, 2020. URL <https://arxiv.org/abs/2006.11239>.
- Koji Hukushima and Koji Nemoto. Exchange monte carlo method and application to spin glass simulations. *Journal of the Physical Society of Japan*, 65(6):1604–1608, June 1996. ISSN 1347-4073. doi: 10.1143/jpsj.65.1604. URL <http://dx.doi.org/10.1143/JPSJ.65.1604>.
- Justin Johnson, Alexandre Alahi, and Li Fei-Fei. Perceptual losses for real-time style transfer and super-resolution, 2016. URL <https://arxiv.org/abs/1603.08155>.
- Ian T. Jolliffe and Jorge Cadima. Principal component analysis: a review and recent developments. *Philosophical Transactions of the Royal Society A: Mathematical, Physical and Engineering Sciences*, 374(2065):20150202, 2016. ISSN 1364-503X. doi: 10.1098/rsta.2015.0202.
- JuliaCI. Benchmarktools.jl, 2024. URL <https://juliaci.github.io/BenchmarkTools.jl/stable/>. Accessed on August 20, 2024.
- George Em Karniadakis, Ioannis G. Kevrekidis, Lu Lu, Paris Perdikaris, Sifan Wang, and Liu Yang. Physics-informed machine learning. *Nature Reviews Physics*, 3(6):422–440, 2021. ISSN 2522-5820. doi: 10.1038/s42254-021-00314-5. URL <https://doi.org/10.1038/s42254-021-00314-5>.
- Diederik P. Kingma and Max Welling. Auto-encoding variational bayes, 2022. URL <https://arxiv.org/abs/1312.6114>. arXiv:1312.6114.
- Diederik P. Kingma, Danilo J. Rezende, Shakir Mohamed, and Max Welling. Semi-supervised learning with deep generative models, 2014. URL <https://arxiv.org/abs/1406.5298>.
- T. Kloek and H. K. van Dijk. Bayesian estimates of equation system parameters: An application of integration by monte carlo. *Econometrica*, 46(1):1–19, 1978. ISSN 00129682, 14680262. URL <http://www.jstor.org/stable/1913641>.
- Deqian Kong, Bo Pang, and Ying Nian Wu. Unsupervised meta-learning via latent space energy-based model of symbol vector coupling. In *Fifth Workshop on Meta-Learning at the Conference on Neural Information Processing Systems*, 2021. URL <https://openreview.net/forum?id=-pLftu7EpXz>.
- R. Larson and B.H. Edwards. *Calculus of a Single Variable*. Cengage Learning, 2008. ISBN 9780547209982. URL [https://books.google.co.uk/books?id=gR7nGg5\\_9xcC](https://books.google.co.uk/books?id=gR7nGg5_9xcC).
- Chris Lattner, Mehdi Amini, Uday Bondhugula, Albert Cohen, Andy Davis, Jacques Pienaar, River Riddle, Tatiana Shpeisman, Nicolas Vasilache, and Oleksandr Zinenko. Mlir: A compiler infrastructure for the end of moore’s law, 2020. URL <https://arxiv.org/abs/2002.11054>.
- Dirk Laurie. Calculation of gauss-kronrod quadrature rules. *Math. Comput.*, 66:1133–1145, 07 1997. doi: 10.1090/S0025-5718-97-00861-2.
- Yann LeCun, Yoshua Bengio, and Geoffrey Hinton. Deep learning. *Nature*, 521(7553):436–444, May 28 2015. ISSN 1476-4687. doi: 10.1038/nature14539.
- Ziyao Li. Kolmogorov-arnold networks are radial basis function networks, 2024. URL <https://arxiv.org/abs/2405.06721>.
- Ziming Liu, Yixuan Wang, Sachin Vaidya, Fabian Ruehle, James Halverson, Marin Soljačić, Thomas Y. Hou, and Max Tegmark. Kan: Kolmogorov-arnold networks, 2024. URL <https://arxiv.org/abs/2404.19756>.
- Ziwei Liu, Ping Luo, Xiaogang Wang, and Xiaoou Tang. Deep learning face attributes in the wild, 2015. URL <https://arxiv.org/abs/1411.7766>.
- E. Marinari and G. Parisi. Simulated tempering: A new monte carlo scheme. *Europhysics Letters*, 19(6):451, jul 1992. doi: 10.1209/0295-5075/19/6/002. URL <https://dx.doi.org/10.1209/0295-5075/19/6/002>.

- Nicholas Metropolis and S. Ulam. The monte carlo method. *Journal of the American Statistical Association*, 44(247):335–341, 1949. ISSN 01621459, 1537274X. URL <http://www.jstor.org/stable/2280232>.
- William Moses and Valentin Churavy. Instead of rewriting foreign code for machine learning, automatically synthesize fast gradients. In *Advances in Neural Information Processing Systems*, volume 33, pp. 12472–12485. Curran Associates, Inc., 2020.
- William S. Moses, Valentin Churavy, Ludger Paehler, Jan Hückelheim, Sri Hari Krishna Narayanan, Michel Schanen, and Johannes Doerfert. Reverse-mode automatic differentiation and optimization of gpu kernels via enzyme. In *Proceedings of the International Conference for High Performance Computing, Networking, Storage and Analysis*. Association for Computing Machinery, 2021.
- William S. Moses, Sri Hari Krishna Narayanan, Ludger Paehler, Valentin Churavy, Michel Schanen, Jan Hückelheim, Johannes Doerfert, and Paul Hovland. Scalable automatic differentiation of multiple parallel paradigms through compiler augmentation. In *Proceedings of the International Conference on High Performance Computing, Networking, Storage and Analysis*. IEEE Press, 2022.
- Fionn Murtagh. Multilayer perceptrons for classification and regression. *Neurocomputing*, 2(5):183–197, 1991. ISSN 0925-2312. doi: [https://doi.org/10.1016/0925-2312\(91\)90023-5](https://doi.org/10.1016/0925-2312(91)90023-5). URL <https://www.sciencedirect.com/science/article/pii/0925231291900235>.
- Radford M. Neal. Annealed importance sampling, 1998. URL <https://arxiv.org/abs/physics/9803008>.
- Yuval Netzer, Tao Wang, Adam Coates, Alessandro Bissacco, Bo Wu, and Andrew Y. Ng. Reading digits in natural images with unsupervised feature learning. In *NIPS Workshop on Deep Learning and Unsupervised Feature Learning 2011*, 2011. URL [http://ufldl.stanford.edu/housenumbers/nips2011\\_housenumbers.pdf](http://ufldl.stanford.edu/housenumbers/nips2011_housenumbers.pdf).
- Erik Nijkamp, Mitch Hill, Tian Han, Song-Chun Zhu, and Ying Nian Wu. On the anatomy of mcmc-based maximum likelihood learning of energy-based models, 2019a. URL <https://arxiv.org/abs/1903.12370>.
- Erik Nijkamp, Mitch Hill, Song-Chun Zhu, and Ying Nian Wu. Learning non-convergent non-persistent short-run mcmc toward energy-based model, 2019b. URL <https://arxiv.org/abs/1904.09770>.
- Bo Pang, Tian Han, Erik Nijkamp, Song-Chun Zhu, and Ying Nian Wu. Learning latent space energy-based prior model, 2020. URL <https://arxiv.org/abs/2006.08205>.
- George Papamakarios, Eric Nalisnick, Danilo Jimenez Rezende, Shakir Mohamed, and Balaji Lakshminarayanan. Normalizing flows for probabilistic modeling and inference, 2021. URL <https://arxiv.org/abs/1912.02762>.
- T. Poggio and F. Girosi. Networks for approximation and learning. *Proceedings of the IEEE*, 78(9): 1481–1497, 1990. doi: 10.1109/5.58326. URL <https://doi.org/10.1109/5.58326>.
- Mariano Rivera. How to train your vae, 2024. URL <https://arxiv.org/abs/2309.13160>.
- G. O. Roberts and O. Stramer. Langevin diffusions and metropolis-hastings algorithms. *Methodology and Computing in Applied Probability*, 4(4):337–357, 2002. ISSN 1573-7713. doi: 10.1023/A:1023562417138. URL <https://doi.org/10.1023/A:1023562417138>.
- P. J. Rossky, J. D. Doll, and H. L. Friedman. Brownian dynamics as smart monte carlo simulation. *The Journal of Chemical Physics*, 69(10):4628–4633, 11 1978a. ISSN 0021-9606. doi: 10.1063/1.436415. URL <https://doi.org/10.1063/1.436415>.
- P. J. Rossky, J. D. Doll, and H. L. Friedman. Brownian dynamics as smart monte carlo simulation. *The Journal of Chemical Physics*, 69(10):4628–4633, 1978b. doi: 10.1063/1.436415.

Karen Simonyan and Andrew Zisserman. Very deep convolutional networks for large-scale image recognition, 2015. URL <https://arxiv.org/abs/1409.1556>.

Robert Swendsen and Jian-Sheng Wang. Replica monte carlo simulation of spin-glasses. *Physical review letters*, 57:2607–2609, 12 1986. doi: 10.1103/PhysRevLett.57.2607.

Christian Szegedy, Vincent Vanhoucke, Sergey Ioffe, Jonathon Shlens, and Zbigniew Wojna. Re-thinking the inception architecture for computer vision, 2015.

Joshua Wilkie. Numerical methods for stochastic differential equations. *Physical Review E*, 70(1), July 2004. ISSN 1550-2376. doi: 10.1103/physreve.70.017701. URL <http://dx.doi.org/10.1103/PhysRevE.70.017701>.

Han Xiao, Kashif Rasul, and Roland Vollgraf. Fashion-mnist: a novel image dataset for benchmarking machine learning algorithms, 2017. URL <https://arxiv.org/abs/1708.07747>.

Shiyu Yuan, Jiali Cui, Hanao Li, and Tian Han. Learning multimodal latent generative models with energy-based prior, 2024. URL <https://arxiv.org/abs/2409.19862>.

Zetta. Zetta, the next paradigm of sustainable computing. <https://zsc.ai/litepaper>, August 2024. The Zettascale Computing Corp. introduce a polymorphic computing chip technology, achieving up to 27.6x efficiency gains over the H100 GPUs through dynamically reconfigurable hardware that adapts to diverse AI models via software configuration.

Xinwei Zhang, Zhiqiang Tan, and Zhijian Ou. Persistently trained, diffusion-assisted energy-based models, 2023. URL <https://arxiv.org/abs/2304.10707>.

## A APPENDIX

### A.1 CODEBASE

The study was implemented at <https://github.com/thezettascale/KAEM>.

### A.2 COMPUTATIONAL BENCHMARKS

These benchmarks were collected for FP32 on a GPU (NVIDIA GeForce RTX 4060) with Julia’s BenchmarkTools package, (JuliaCI, 2024). Compilation and reverse differentiation were performed using Julia’s Reactant (EnzymeAD & Reactant.jl Contributors, 2025) and Enzyme (Moses & Churavy, 2020; Moses et al., 2021; 2022) packages.

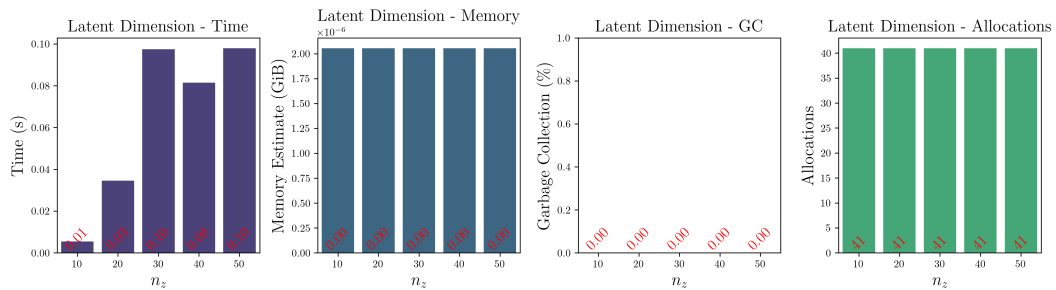


Figure 7: Benchmarks for varying latent dimensions,  $n_z$ , while sampling from independent EBM priors with ITS and estimating posterior expectations with IS. The prior had an input size of  $n_z$  and an output size of  $2n_z + 1$ . The generator received inputs of size  $2n_z + 1$ , with a hidden size of  $4n_z + 2$  and an output size of  $28 \times 28$ . All other hyperparameters were consistent with Tab. 4 (RBF bases). They reflect the performance of a reverse autodifferentiation of the MLE criterion, Eq. 16.

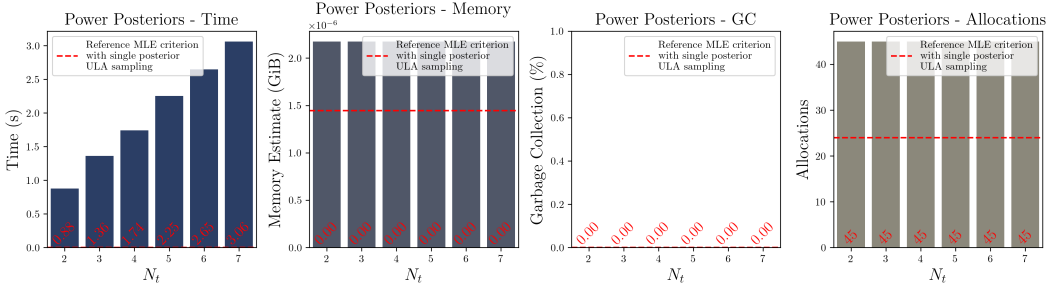


Figure 8: Benchmarks for varying amounts of temperatures,  $N_t$ , using a mixture of EBM priors (Tab. 6) with ITS sampling. Posterior expectations were estimated with SE and population-based ULA. All other hyperparameters were kept consistent with Tab. 5 (Celeb-A). They reflect the computational cost of performing a single reverse autodifferentiation of the SE criterion, Eq. 31.

### A.3 GUIDANCE ON TEMPERING

#### A.3.1 CYCLIC ANNEALING

Calderhead & Girolami (2009) demonstrated that uniformly scheduling the discretized temperatures in Eq. 30 results in unequal contributions of adjacent power posteriors to the Thermodynamic Integral. The success of TI and SE, relies on selecting each  $t_k$  to ensure sufficient overlap of adjacent power posteriors. This overlap ensures similarity between adjacent power posteriors, as introduced in Sec. A.5.1, which influences the Monte Carlo estimator in Eq. 32, given that SE is an application of importance sampling, (Annis et al., 2019).

This overlap is quantified by the KL divergence term in Eq. 50. Maintaining small KL divergences between adjacent power posteriors can be achieved by clustering temperatures in regions where  $\mathbb{P}(\mathbf{z} | \mathbf{x}^{(b)}, \mathbf{f}, \Phi, t_k)$  changes rapidly. To accomplish this, we follow Calderhead & Girolami (2009) in adopting a power-law relationship to schedule the temperatures of Eq. 30:

$$t_k = \left( \frac{k}{N_t} \right)^p, \quad k = 0, 1, \dots, N_t, \quad (35)$$

The effect of varying  $p$  on the schedule between 0 and 1 is visualized in Fig. 9. When  $p > 1$ , spacing becomes denser near  $t = 0$ , while  $p < 1$  creates denser spacing near  $t = 1$ . The impact of varying  $p$  on the discretized Thermodynamic Integral of Eq. 50 is illustrated in Fig. 10. The plots demonstrate that for  $p > 1$ , the trapezoidal bins are clustered closer to  $t = 0$ , concentrating the discrete approximation error towards  $t = 1$ .

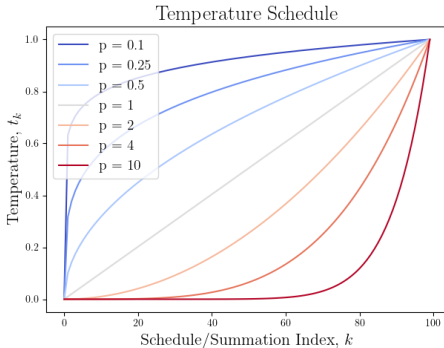


Figure 9: Power-law schedule.

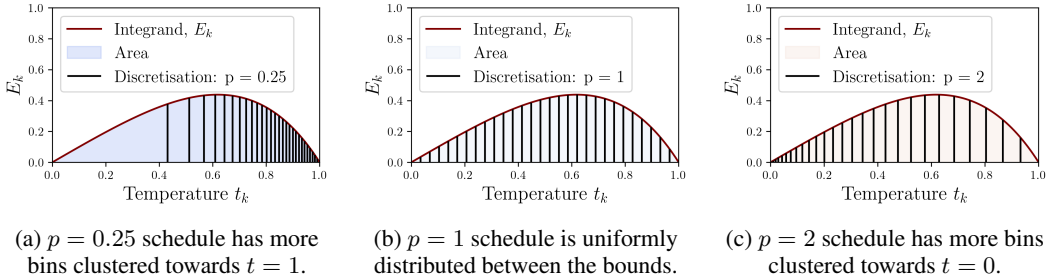


Figure 10: Effect of power-law schedule clusters on integral approximation error. Evaluation points can be skewed towards a particular bound by choosing  $p$ . Increasing  $p$  provides more tempering, concentrating more evaluation points on smoother likelihoods. Tempering helps to mitigate practical challenges associated with the non-smoothness of the univariate functions in Eq. 1.

The study by Calderhead & Girolami (2009) derives an analytic term for an optimal tempering distribution in the context of linear regression models, where the power posterior in Eq. 29 is used to evaluate the plausibility of model parameters in relation to the data, rather than reflecting a latent variable posterior. However, their findings may not hold in the context of KAEM and generative modeling, making  $p$  and the temperature schedule difficult variables to tune.

Instead, we schedule  $p$  sinusoidally across all training parameter updates, starting with a lower value of  $p$  and ending with a higher value, treated as tunable hyperparameters.

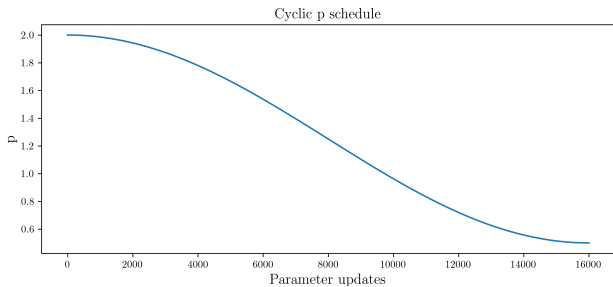


Figure 11: Cosine  $p$  schedule, decreasing from 2 to 0.5

Initializing  $p > 1$  focuses learning on low-variance, smoother power posteriors during the early stages of the cycle, where global features emerge between adjacent power posteriors. As training progresses, KAEM will have learned the global features sufficiently well, reducing the change of density between adjacent power posteriors of a  $p > 1$  schedule. At this stage,  $p(i)$  will have transitioned to  $p \leq 1$ , thereby shifting KAEM’s focus towards capturing more high-variance, data-informed features of the posterior landscape, where training is expected to enhance its ability to generate finer details.

Guidance on selecting optimal values for the tempering hyperparameters is provided in Tab. 3.

## A.3.2 CHOOSING HYPERPARAMETERS

Table 3: Tempering hyperparameters.

Hyperparameter	Description
$N_t > 1$	Specifies the number of power posteriors, enabling a smooth transition between the prior and posterior. Increasing this improves exploration but also increases cost due to the need for more MALA iterations. Typically, this is memory-bound and guided by hardware availability, such as $N_t = 5$ .
$N_{\text{local}} > 1$	Determines the number of ULA or autoMALA iterations per posterior. Although increasing this value improves the quality of samples at each stage, it also raises the computational cost, much like $N_t$ . It can be kept at a small value, such as $N_{\text{local}} = 40$ , (based on the recommendations of Nijkamp et al. (2019b;a) regarding short-run Markov chain Monte Carlo).
$N_{\text{unadjusted}} > 1$	Controls the number of autoMALA iterations performed without MH adjustments, reflecting the level of exploration at each power posterior. This can be set to 1, as guided by Biron-Lattes et al. (2024).
$p_{\text{init}} > 1, p_{\text{end}} \leq 1, N_{\text{cycles}} \geq 0$	Controls the evolution of tempering during training. If the data is expected to have smooth relationships, reduce both $p_{\text{init}}$ and $p_{\text{end}}$ . For data with finer details, increase both values to allow for better focus on capturing intricate features. The values used for this study were $p_{\text{init}} = 3$ , and $p_{\text{end}} = 1$ , since our experience suggests that power posteriors initially change rapidly closer to the prior. The number of cycles, $N_{\text{cycles}}$ , controls the periodicity of cosine scheduling similar to cyclic annealing (Fu et al., 2019).

## A.4 DERIVATIONS AND OTHER IDENTITIES

## A.4.1 USEFUL PROOF

The following short proof for a learning gradient with respect to an arbitrary set of parameters,  $\theta$ , proves useful for other derivations in this study:

$$\begin{aligned} \mathbb{E}_{p_{\theta}(\mathbf{x})} [\nabla_{\theta} \log p_{\theta}(\mathbf{x})] &= \mathbb{E}_{p_{\theta}(\mathbf{x})} \left[ \frac{\nabla_{\theta} p_{\theta}(\mathbf{x})}{p_{\theta}(\mathbf{x})} \right] = \int_{\mathcal{X}} \frac{\nabla_{\theta} p_{\theta}(\mathbf{x})}{p_{\theta}(\mathbf{x})} dp_{\theta}(\mathbf{x}) \\ &= \int_{\mathcal{X}} \nabla_{\theta} p_{\theta}(\mathbf{x}) d\mathbf{x} = \nabla_{\theta} \int_{\mathcal{X}} p_{\theta}(\mathbf{x}) d\mathbf{x} = \nabla_{\theta} 1 = 0. \end{aligned} \quad (36)$$

## A.4.2 MARGINAL LIKELIHOOD

$$\begin{aligned} \log \left( p_{f, \Phi}(\mathbf{x}^{(b)}) \right) &= \mathbb{E}_{p_{f, \Phi}(\mathbf{z} | \mathbf{x}^{(b)})} \left[ \log \left( p_{f, \Phi}(\mathbf{x}^{(b)}, \mathbf{z}) \right) \right] \\ &= \mathbb{E}_{p_{f, \Phi}(\mathbf{z} | \mathbf{x}^{(b)})} \left[ \log \left( p_f(\mathbf{z}) \cdot p_{\Phi}(\mathbf{x}^{(b)} | \mathbf{z}) \right) \right] \\ &= \mathbb{E}_{p_{f, \Phi}(\mathbf{z} | \mathbf{x}^{(b)})} \left[ \log(p_f(\mathbf{z})) + \log \left( p_{\Phi}(\mathbf{x}^{(b)} | \mathbf{z}) \right) \right]. \end{aligned} \quad (37)$$

## A.4.3 MAXIMUM LIKELIHOOD LEARNING GRADIENT

This proof demonstrates that the learning gradient with respect to an arbitrary set of parameters,  $\theta$ , is independent of sampling:

$$\begin{aligned} \mathbb{E}_{p(\mathbf{z} | \mathbf{x})} [\nabla_{\theta} \log p(\mathbf{x}, \mathbf{z})] &= \mathbb{E}_{p(\mathbf{z} | \mathbf{x})} [\nabla_{\theta} \log p(\mathbf{z} | \mathbf{x}) + \nabla_{\theta} \log p(\mathbf{x})] \\ &= \mathbb{E}_{p(\mathbf{z} | \mathbf{x})} [\nabla_{\theta} \log p(\mathbf{z} | \mathbf{x})] + \mathbb{E}_{p(\mathbf{z} | \mathbf{x})} [\nabla_{\theta} \log p(\mathbf{x})] \\ &= 0 + \nabla_{\theta} \log p(\mathbf{x}), \end{aligned} \quad (38)$$

where Eq. 36 has been used to zero the expected posterior. This allows gradient flow to be disregarded in sampling procedures as shown in Eq. 16.

#### A.4.4 CONTRASTIVE DIVERGENCE LEARNING GRADIENT FOR LOG-PRIOR

The learning gradient attributed to the prior can be derived into a contrastive divergence framework, which is more typical of energy-based modeling literature. The prior model is solely dependent on  $f$  in Eq. 4. We can rewrite Eq. 17 as:

$$\nabla_{\mathbf{f}} \log(p_{\mathbf{f}}(\mathbf{z})) = \nabla_{\mathbf{f}} \sum_{q=1}^{2n_z+1} \sum_{p=1}^{n_z} \log(\pi_{q,p}(z_{q,p})) = \nabla_{\mathbf{f}} \sum_{q=1}^{2n_z+1} \sum_{p=1}^{n_z} f_{q,p}(z_{q,p}) + \log(\pi_0(z_{q,p})) - \log(Z_{q,p}) \quad (39)$$

where  $Z_{q,p} = \int_{\mathcal{Z}} \exp(f_{q,p}(z_p)) d\pi_0(z_p)$  is the normalization constant. We can simplify the constant using Eq. 36:

$$\begin{aligned} \mathbb{E}_{p_{\mathbf{f}}(\mathbf{z})} \left[ \nabla_{\mathbf{f}} \log p_{\mathbf{f}}(\mathbf{z}) \right] &= \mathbb{E}_{p_{\mathbf{f}}(\mathbf{z})} \left[ \nabla_{\mathbf{f}} \sum_{q=1}^{2n_z+1} \sum_{p=1}^{n_z} f_{q,p}(z_{q,p}) + \log(\pi_0(z_{q,p})) - \log(Z_{q,p}) \right] = 0 \\ &= \mathbb{E}_{p_{\mathbf{f}}(\mathbf{z})} \left[ \nabla_{\mathbf{f}} \sum_{q=1}^{2n_z+1} \sum_{p=1}^{n_z} f_{q,p}(z_{q,p}) \right] - \nabla_{\mathbf{f}} \sum_{q=1}^{2n_z+1} \sum_{p=1}^{n_z} \log(Z_{q,p}) = 0 \\ \therefore \nabla_{\mathbf{f}} \sum_{q=1}^{2n_z+1} \sum_{p=1}^{n_z} \log(Z_{q,p}) &= \mathbb{E}_{p_{\mathbf{f}}(\mathbf{z})} \left[ \nabla_{\mathbf{f}} \sum_{q=1}^{2n_z+1} \sum_{p=1}^{n_z} f_{q,p}(z_{q,p}) \right] \end{aligned} \quad (40)$$

Therefore the log-prior gradient of Eq. 39 can be evaluated without quadrature normalization as:

$$\nabla_{\mathbf{f}} \log p_{\mathbf{f}}(\mathbf{z}) = \nabla_{\mathbf{f}} \sum_{q=1}^{2n_z+1} \sum_{p=1}^{n_z} f_{q,p}(z_{q,p}) - \mathbb{E}_{p_{\mathbf{f}}(\mathbf{z})} \left[ \nabla_{\mathbf{f}} \sum_{q=1}^{2n_z+1} \sum_{p=1}^{n_z} f_{q,p}(z_{q,p}) \right], \quad (41)$$

and the learning gradient attributed to the prior is finalized into a contrastive divergence format:

$$\begin{aligned} \mathbb{E}_{p_{\mathbf{f},\Phi}(\mathbf{z}|\mathbf{x})} \left[ \nabla_{\mathbf{f}} [\log p_{\mathbf{f}}(\mathbf{z})] \right] &= \mathbb{E}_{p_{\mathbf{f},\Phi}(\mathbf{z}|\mathbf{x})} \left[ \nabla_{\mathbf{f}} \sum_{q=1}^{2n_z+1} \sum_{p=1}^{n_z} f_{q,p}(z_{q,p}) \right] \\ &\quad - \mathbb{E}_{p_{\mathbf{f}}(\mathbf{z})} \left[ \nabla_{\mathbf{f}} \sum_{q=1}^{2n_z+1} \sum_{p=1}^{n_z} f_{q,p}(z_{q,p}) \right]. \end{aligned} \quad (42)$$

#### A.4.5 DERIVING THE THERMODYNAMIC INTEGRAL

Starting from the power posterior:

$$p_{\mathbf{f},\Phi}(\mathbf{z} | \mathbf{x}^{(b)}, t) = \frac{p_{\Phi}(\mathbf{x}^{(b)} | \mathbf{z})^t p_{\mathbf{f}}(\mathbf{z})}{\mathbf{Z}_t} \quad (43)$$

The partition function  $\mathbf{Z}_t$  is given by:

$$\mathbf{Z}_t = \mathbb{E}_{p_{\mathbf{f}}(\mathbf{z})} \left[ p_{\Phi}(\mathbf{x}^{(b)} | \mathbf{z})^t \right] \quad (44)$$

Now, differentiating the log-partition function with respect to  $t$ :

$$\begin{aligned} \frac{\partial}{\partial t} \log(\mathbf{Z}_t) &= \frac{1}{\mathbf{Z}_t} \frac{\partial}{\partial t} \mathbf{Z}_t = \frac{1}{\mathbf{Z}_t} \mathbb{E}_{p_{\mathbf{f}}(\mathbf{z})} \left[ \frac{\partial}{\partial t} p_{\Phi}(\mathbf{x}^{(b)} | \mathbf{z})^t \right] \\ &= \frac{1}{\mathbf{Z}_t} \mathbb{E}_{p_{\mathbf{f}}(\mathbf{z})} \left[ \log p_{\Phi}(\mathbf{x}^{(b)} | \mathbf{z}) \cdot p_{\Phi}(\mathbf{x}^{(b)} | \mathbf{z})^t \right] \\ &= \mathbb{E}_{p_{\mathbf{f},\Phi}(\mathbf{z}|\mathbf{x}^{(b)},t)} \left[ \log p_{\Phi}(\mathbf{x}^{(b)} | \mathbf{z}) \right] \end{aligned} \quad (45)$$

Integrating both sides from 0 to 1:

$$\int_0^1 \frac{\partial}{\partial t} \log(\mathbf{Z}_t) dt = \int_0^1 \mathbb{E}_{p_{\mathbf{f}, \Phi}(\mathbf{z} | \mathbf{x}^{(b)}, t)} \left[ \log p_{\Phi}(\mathbf{x}^{(b)} | \mathbf{z}) \right] dt \quad (46)$$

Using the fundamental theorem of calculus, (Larson & Edwards, 2008):

$$\int_0^1 \frac{\partial}{\partial t} \log(\mathbf{Z}_t) dt = \log(\mathbf{Z}_{t=1}) - \log(\mathbf{Z}_{t=0}) = \int_0^1 \mathbb{E}_{p_{\mathbf{f}, \Phi}(\mathbf{z} | \mathbf{x}^{(b)}, t)} \left[ \log p_{\Phi}(\mathbf{x}^{(b)} | \mathbf{z}) \right] dt \quad (47)$$

The limits of the integrals can be expressed as:

$$\begin{aligned} \log(\mathbf{Z}_{t=0}) &= \log \left( \mathbb{E}_{p_{\mathbf{f}}(\mathbf{z})} \left[ p_{\Phi}(\mathbf{x}^{(b)} | \mathbf{z})^0 \right] \right) = \log(1) = 0 \\ \log(\mathbf{Z}_{t=1}) &= \log \left( \mathbb{E}_{p_{\mathbf{f}, \Phi}(\mathbf{z} | \mathbf{x}^{(b)})} \left[ \log p_{\Phi}(\mathbf{x}^{(b)} | \mathbf{z}) \right] \right) = \log \mathbb{P}(\mathbf{x}^{(b)} | \mathbf{f}, \Phi) \end{aligned} \quad (48)$$

Therefore, we obtain the log-marginal likelihood expressed as the Thermodynamic Integral:

$$\log(\mathbf{Z}_{t=1}) - \log(\mathbf{Z}_{t=0}) = \log \mathbb{P}(\mathbf{x}^{(b)} | \mathbf{f}, \Phi) = \int_0^1 \mathbb{E}_{p_{\mathbf{f}, \Phi}(\mathbf{z} | \mathbf{x}^{(b)}, t)} \left[ \log p_{\Phi}(\mathbf{x}^{(b)} | \mathbf{z}) \right] dt \quad (49)$$

#### A.4.6 DISCRETIZING THE THERMODYNAMIC INTEGRAL

Here,  $t_k$  denotes the tempering at the  $k$ -th index of the schedule, and  $N_t$  is the number of temperatures. As derived by Calderhead & Girolami (2009), Eq. 28 then be evaluated using:

$$\log \left( p_{\mathbf{f}, \Phi}(\mathbf{x}^{(b)}) \right) = \frac{1}{2} \sum_{k=1}^{N_t} \Delta t_k (E_{k-1} + E_k) + \frac{1}{2} \sum_{k=1}^{N_t} D_{\text{KL}}(\mathbb{P}_{t_{k-1}} || \mathbb{P}_{t_k}) - D_{\text{KL}}(\mathbb{P}_{t_k} || \mathbb{P}_{t_{k-1}}) \quad (50)$$

Where:

$$\begin{aligned} \Delta t_k &= t_k - t_{k-1}, \quad E_k = \mathbb{E}_{p_{\mathbf{f}, \Phi}(\mathbf{z} | \mathbf{x}^{(b)}, t_k)} \left[ \log \left( p_{\Phi}(\mathbf{x}^{(b)} | \mathbf{z}) \right) \right], \\ D_{\text{KL}}(\mathbb{P}_{t_{k-1}} || \mathbb{P}_{t_k}) &= \mathbb{E}_{p_{\mathbf{f}, \Phi}(\mathbf{z} | \mathbf{x}^{(b)}, t_{k-1})} \left[ \log \left( \frac{p_{\mathbf{f}, \Phi}(\mathbf{z} | \mathbf{x}^{(b)}, t_{k-1})}{p_{\mathbf{f}, \Phi}(\mathbf{z} | \mathbf{x}^{(b)}, t_k)} \right) \right] \end{aligned} \quad (51)$$

This reflects the trapezium rule for numerical integration, supported by bias correction to provide an estimate of the Riemann integral that is especially robust to error. The learning gradient derived from the discretized Thermodynamic Integral is unchanged from the MLE gradient in Eq. 16, as demonstrated under Sec. A.4.7.

#### A.4.7 LEARNING GRADIENT FOR DISCRETIZED THERMODYNAMIC INTEGRAL AND POWER POSTERIOR PARTITION FUNCTION

We can derive the learning gradient of the discretized Thermodynamic Integral in Eq. 50 by reducing it down into a sum of normalizing constants. Starting from the definitions attributed to the KL divergence terms:

$$\begin{aligned} D_{\text{KL}}(\mathbb{P}_{t_{k-1}} || \mathbb{P}_{t_k}) &= \mathbb{E}_{p_{\mathbf{f}, \Phi}(\mathbf{z} | \mathbf{x}^{(b)}, t_{k-1})} \left[ \log p_{\mathbf{f}, \Phi}(\mathbf{z} | \mathbf{x}^{(b)}, t_{k-1}) - \log p_{\mathbf{f}, \Phi}(\mathbf{z} | \mathbf{x}^{(b)}, t_k) \right] \\ \text{and } D_{\text{KL}}(\mathbb{P}_{t_k} || \mathbb{P}_{t_{k-1}}) &= \mathbb{E}_{p_{\mathbf{f}, \Phi}(\mathbf{z} | \mathbf{x}^{(b)}, t_k)} \left[ \log p_{\mathbf{f}, \Phi}(\mathbf{z} | \mathbf{x}^{(b)}, t_k) - \log p_{\mathbf{f}, \Phi}(\mathbf{z} | \mathbf{x}^{(b)}, t_{k-1}) \right] \\ &= -\mathbb{E}_{p_{\mathbf{f}, \Phi}(\mathbf{z} | \mathbf{x}^{(b)}, t_k)} \left[ \log p_{\mathbf{f}, \Phi}(\mathbf{z} | \mathbf{x}^{(b)}, t_{k-1}) - \log p_{\mathbf{f}, \Phi}(\mathbf{z} | \mathbf{x}^{(b)}, t_k) \right] \end{aligned} \quad (52)$$

We can leverage Eq. 29 to quantify the log-difference in terms of the change in likelihood contribution plus some normalization constant:

$$\log p_{\mathbf{f}, \Phi}(\mathbf{z} | \mathbf{x}^{(b)}, t_{k-1}) - \log p_{\mathbf{f}, \Phi}(\mathbf{z} | \mathbf{x}^{(b)}, t_k) = -\Delta t_k \cdot \log p_{\Phi}(\mathbf{x}^{(b)} | \mathbf{z}) + \log \left( \frac{\mathbf{Z}_{t_k}}{\mathbf{Z}_{t_{k-1}}} \right) \quad (53)$$

The definitions in Eq. 51 can be used to express the KL divergences in terms of the expected likelihoods:

$$\begin{aligned} \therefore D_{\text{KL}}(\mathbb{P}_{t_{k-1}} \|\mathbb{P}_{t_k}) &= -\Delta t_k \cdot \mathbb{E}_{p_{f, \Phi}(\mathbf{z}|\mathbf{x}^{(b)}, t_{k-1})} \left[ \log p_{\Phi}(\mathbf{x}^{(b)} | \mathbf{z}) \right] + \log \left( \frac{\mathbf{Z}_{t_k}}{\mathbf{Z}_{t_{k-1}}} \right) \\ &= -\Delta t_k \cdot E_{k-1} + \log \left( \frac{\mathbf{Z}_{t_k}}{\mathbf{Z}_{t_{k-1}}} \right) \end{aligned} \quad (54)$$

$$\begin{aligned} \text{and } D_{\text{KL}}(\mathbb{P}_{t_k} \|\mathbb{P}_{t_{k-1}}) &= \Delta t_k \cdot \mathbb{E}_{p_{f, \Phi}(\mathbf{z}|\mathbf{x}^{(b)}, t_k)} \left[ \log p_{\Phi}(\mathbf{x}^{(b)} | \mathbf{z}) \right] - \log \left( \frac{\mathbf{Z}_{t_k}}{\mathbf{Z}_{t_{k-1}}} \right) \\ &= \Delta t_k \cdot E_k - \log \left( \frac{\mathbf{Z}_{t_k}}{\mathbf{Z}_{t_{k-1}}} \right) \end{aligned} \quad (55)$$

Substituting back into Eq. 50, we eliminate the expected likelihood terms:

$$\begin{aligned} \frac{1}{2} \sum_{k=1}^{N_t} D_{\text{KL}}(\mathbb{P}_{t_{k-1}} \|\mathbb{P}_{t_k}) - D_{\text{KL}}(\mathbb{P}_{t_k} \|\mathbb{P}_{t_{k-1}}) &= -\frac{1}{2} \sum_{k=1}^{N_t} \Delta t_k (E_{k-1} + E_k) - 2 \log \left( \frac{\mathbf{Z}_{t_k}}{\mathbf{Z}_{t_{k-1}}} \right) \\ \therefore \log \left( p_{f, \Phi}(\mathbf{x}^{(b)}) \right) &= \frac{1}{2} \sum_{k=1}^{N_t} \Delta t_k (E_{k-1} + E_k) + \frac{1}{2} \sum_{k=1}^{N_t} D_{\text{KL}}(\mathbb{P}_{t_{k-1}} \|\mathbb{P}_{t_k}) - D_{\text{KL}}(\mathbb{P}_{t_k} \|\mathbb{P}_{t_{k-1}}) \\ &= \frac{1}{2} \sum_{k=1}^{N_t} \Delta t_k (E_{k-1} + E_k) - \left[ \frac{1}{2} \sum_{k=1}^{N_t} \Delta t_k (E_{k-1} + E_k) - 2 \log \left( \frac{\mathbf{Z}_{t_k}}{\mathbf{Z}_{t_{k-1}}} \right) \right] \\ &= \sum_{k=1}^{N_t} \log \left( \frac{\mathbf{Z}_{t_k}}{\mathbf{Z}_{t_{k-1}}} \right) = \sum_{k=1}^{N_t} \log(\mathbf{Z}_{t_k}) - \log(\mathbf{Z}_{t_{k-1}}) \end{aligned} \quad (56)$$

Following a similar method to Sec. A.4.4 we can use Eq. 36 to express the learning gradient attributed to each normalization constant in a simpler manner:

$$\begin{aligned} &\mathbb{E}_{p_{f, \Phi}(\mathbf{z}|\mathbf{x}^{(b)}, t_k)} \left[ \nabla_{f, \Phi} \log p_{f, \Phi}(\mathbf{z} | \mathbf{x}^{(b)}, t_k) \right] \\ &= \mathbb{E}_{p_{f, \Phi}(\mathbf{z}|\mathbf{x}^{(b)}, t_k)} \left[ t_k \cdot \nabla_{\Phi} \log p_{\Phi}(\mathbf{x}^{(b)} | \mathbf{z}) + \nabla_f \log p_f(\mathbf{z}) \right] - \nabla_{f, \Phi} \log(\mathbf{Z}_{t_k}) = 0 \\ \therefore \nabla_{f, \Phi} \log(\mathbf{Z}_{t_k}) &= \mathbb{E}_{p_{f, \Phi}(\mathbf{z}|\mathbf{x}^{(b)}, t_k)} \left[ t_k \cdot \nabla_{\Phi} \log p_{\Phi}(\mathbf{x}^{(b)} | \mathbf{z}) + \nabla_f \log p_f(\mathbf{z}) \right] \end{aligned} \quad (57)$$

Telescoping the sum in Eq. 56, and noting that  $k = 1$  corresponds to the power posterior equaling the prior, and  $k = N_t$  to the posterior, Eq. 56 yields KAEM's learning gradient:

$$\begin{aligned} \nabla_{f, \Phi} \log \left( p_{f, \Phi}(\mathbf{x}^{(b)}) \right) &= \sum_{k=1}^{N_t} \nabla_{f, \Phi} \log(\mathbf{Z}_{t_k}) - \nabla_{f, \Phi} \log(\mathbf{Z}_{t_{k-1}}) \\ &= \nabla_{f, \Phi} \log(\mathbf{Z}_{t_{N_t}}) - \nabla_{f, \Phi} \log(\mathbf{Z}_{t_0}) \\ &= \mathbb{E}_{p_{f, \Phi}(\mathbf{z}|\mathbf{x}^{(b)})} \left[ \nabla_f \log p_f(\mathbf{z}) + \nabla_{\Phi} \log p_{\Phi}(\mathbf{x}^{(b)} | \mathbf{z}) \right] \\ &\quad - \underbrace{\mathbb{E}_{\mathbb{P}(\mathbf{z}|f)} \left[ \nabla_f [\log p_f(\mathbf{z})] \right]}_{=0 \text{ (Eq. 36)}}. \end{aligned} \quad (58)$$

## A.5 SAMPLING THEORY

This section provides more theoretical detail regarding KAEM's sampling procedures.

### A.5.1 IMPORTANCE SAMPLING

Importance Sampling (IS) is a Monte Carlo method that enables the estimation of expectations with respect to one probability measure using samples drawn from another. For a detailed exposition, see Kloek & van Dijk (1978).

#### The Radon-Nikodym derivative

IS involves rewriting the expectation of an arbitrary function or density,  $\rho(\mathbf{z})$ , under the target measure,  $\mathbb{P}(\mathbf{z})$ , in terms of a more tractable proposal measure,  $q(\mathbf{z})$ . Specifically, we use the Radon-Nikodym derivative  $\frac{d\mathbb{P}}{d\mathbb{Q}}$  to rewrite the expectation of an arbitrary function of  $\mathbf{z}$ , denoted as  $\rho(\mathbf{z})$ :

$$\mathbb{E}_{\mathbb{P}(\mathbf{z})}[\rho(\mathbf{z})] = \int_{\bar{\mathcal{Z}}} \rho(\mathbf{z}) \mathbb{P}(d\mathbf{z}) = \int_{\bar{\mathcal{Z}}} \rho(\mathbf{z}) \cdot \frac{d\mathbb{P}}{d\mathbb{Q}} \mathbb{Q}(d\mathbf{z}). \quad (59)$$

Here,  $\frac{d\mathbb{P}}{d\mathbb{Q}}$  acts as a weight that adjusts the contribution of each sample to account for the difference between the target and proposal measures. This requires that the proposal measure  $\mathbb{Q}$  is absolutely continuous with respect to the target measure  $\mathbb{P}$ , i.e.  $\mathbb{Q}(A) = 0$  implies  $\mathbb{P}(A) = 0$ , for every measurable subset  $A \in \mathcal{Z}$ .

In the context of KAEM, the target distribution is the posterior,  $p_{f, \Phi}(\mathbf{z} | \mathbf{x}^{(b)})$ , which is proportional to the product of the likelihood and the prior:

$$p_{f, \Phi}(\mathbf{z} | \mathbf{x}^{(b)}) \propto p_{\Phi}(\mathbf{x}^{(b)} | \mathbf{z}) \cdot p_f(\mathbf{z}). \quad (60)$$

The exact normalization constant, (the marginal likelihood  $p_{f, \Phi}(\mathbf{x}^{(b)})$ ), is intractable, but Importance Sampling circumvents the need to compute it explicitly. Instead, the expectation of  $\rho(\mathbf{z})$  under the posterior can be expressed as:

$$\mathbb{E}_{p_{f, \Phi}(\mathbf{z} | \mathbf{x}^{(b)})}[\rho(\mathbf{z})] = \int_{\bar{\mathcal{Z}}} \rho(\mathbf{z}) w(\mathbf{z}) \mathbb{Q}(d\mathbf{z}), \quad (61)$$

where the importance weights  $w(\mathbf{z})$  are given by:

$$w(\mathbf{z}) = \frac{p_{f, \Phi}(\mathbf{z} | \mathbf{x}^{(b)})}{q(\mathbf{z})} = \frac{p_{\Phi}(\mathbf{x}^{(b)} | \mathbf{z}) \cdot p_f(\mathbf{z})}{q(\mathbf{z})}. \quad (62)$$

#### Proposal distribution and importance weights

A practical choice for the proposal density  $q(\mathbf{z})$  is the prior,  $p_f(\mathbf{z})$ , given the availability of draws from the prior using the method outlined in Sec. 2.4.3. This simplifies the importance weights, as the prior has a tractable form and covers the support of the posterior. This yields:

$$w(\mathbf{z}^{(s)}) = p_{\Phi}(\mathbf{x}^{(b)} | \mathbf{z}^{(s)}) \propto \exp(\log(p_{\Phi}(\mathbf{x}^{(b)} | \mathbf{z}^{(s)}))). \quad (63)$$

This reflects that the likelihood now directly informs how much weight to assign to each sample  $\mathbf{z}$ . Intuitively, samples that better explain the observed data  $\mathbf{x}^{(b)}$ , (as measured by the likelihood), are given higher importance. Using the definition of softmax, the normalized weights are given by:

$$\frac{w(\mathbf{z}^{(s)})}{\sum_{r=1}^{N_s} w(\mathbf{z}^{(r)})} = \text{softmax}_s \left( \log(p_{\Phi}(\mathbf{x}^{(b)} | \mathbf{z}^{(s)})) \right). \quad (64)$$

#### Resampling

The suitability of these weights depends on how well  $q(\mathbf{z})$  matches the posterior. In KAEM, there is likely to be significant mismatch due to the complexity of the likelihood models described in Eq. 20. Consequently, the weights will exhibit high variance, resulting in many samples contributing minimally. This reduces the Effective Sample Size (ESS) and introduces bias into the estimates.

To address this, the weights are resampled before proceeding with the posterior expectation. This is accomplished by using one of the methods outlined by Douc et al. (2005), whenever the ESS falls below a certain threshold determined by Eq. 26. Resampling redistributes the sample weights, creating a new population with uniformly distributed weights while preserving the statistical properties of the original distribution. As training progresses and the prior becomes a better match for the posterior, the need for resampling decreases.

After resampling, the corresponding weights will be uniformly distributed and a standard Monte Carlo estimator can be applied instead of the IS estimator.

### Importance Sampling estimator

To estimate the expectation, we draw  $N_s$  independent samples  $\{\mathbf{z}^{(s)}\}_{s=1}^{N_s} \sim q(\mathbf{z})$  using the procedure outlined in Sec. 2.4.3 and compute a weighted sum:

$$\mathbb{E}_{p_{f, \Phi}(\mathbf{z}|\mathbf{x}^{(b)})}[\rho(\mathbf{z})] \approx \sum_{s=1}^{N_s} \rho(\mathbf{z}^{(s)}) \cdot w_{\text{norm}}(\mathbf{z}^{(s)}) \quad (65)$$

$$\approx \frac{1}{N_s} \sum_{s=1}^{N_s} \rho(\mathbf{z}_{\text{resampled}}^{(s)}). \quad (66)$$

The estimator is unbiased, implying that its expectation matches the true posterior expectation. As  $N_s \rightarrow \infty$ , the approximation converges almost surely to the true value, provided that  $q(\mathbf{z})$  sufficiently covers the posterior to ensure a well-conditioned Radon-Nikodym derivative. This estimator is used for the log-marginal likelihood and its gradient in Eqs. 15 & 16, since it provides a means of estimating expectations with respect to the posterior distribution.

### A.5.2 RESIDUAL RESAMPLING

In this study, we adopted residual resampling to filter the population of latent samples whenever the effective sample size (ESS) criterion in Eq. 26 is satisfied. Given a set of normalized weights  $\{w_{\text{norm}}(\mathbf{z}^{(s)})\}_{s=1}^N$ , the method deterministically replicates samples according to the integer part of  $Nw_{\text{norm}}$ , and uses multinomial sampling to allocate the remaining draws according to the residual mass.

1. **Integer replication:** Each sample  $s$  is deterministically replicated

$$r_s = \lfloor N w_{\text{norm}}(\mathbf{z}^{(s)}) \rfloor, \quad (67)$$

resulting in  $\sum_{s=1}^N r_s$  allocated indices.

2. **Residual weights:** The number of remaining draws is

$$R = N - \sum_{s=1}^N r_s. \quad (68)$$

The unallocated probability mass (fractional remainder) is computed as

$$m_s = N w_{\text{norm}}(\mathbf{z}^{(s)}) - r_s. \quad (69)$$

If  $R > 0$ , the residual weights are obtained by normalizing this mass:

$$w_{\text{residual}}(\mathbf{z}^{(s)}) = \frac{m_s}{R}, \quad (70)$$

otherwise  $w_{\text{residual}}(\mathbf{z}^{(s)}) = 0$  for all  $s$ .

3. **Multinomial allocation:** The remaining  $R$  indices are sampled according to the cumulative distribution function of the residual weights. For each draw,

$$k^* = \min \left\{ j \mid \sum_{s=1}^j w_{\text{residual}}(\mathbf{z}^{(s)}) \geq u_i \right\} \quad \text{where } u_i \sim \mathcal{U}([0, 1]). \quad (71)$$

The final resampled index set consists of the deterministic replications given by  $\{r_s\}$  and the stochastic residual allocations drawn from Eq. 71. After resampling, weights are reset to a uniform distribution and a standard Monte Carlo estimator can be used.

## A.6 HYPERPARAMETERS AND TRAINING DETAILS

Table 4: Hyperparameters for Sec. 3.1.1.

<b>EBM Prior</b>		
layer_widths	$p, q$	40, 81
spline_type	(-)	RBF
spline_activation	(-)	Relu
layer_norm	(-)	false
quadrature_method	(-)	gausslegendre
spline_degree	$d$	3
grid_size	$N_{\text{grid}}$	20
grid_update_ratio	$\alpha_{\text{grid}}$	0.05
Initial grid_range (before grid updating)	$[z_{\min}, z_{\max}]$	Uniform: $[0, 1]$ Gaussian: $[-1.5, 1.5]$ No ref.: $[-1.2, 1.2]$
Spline basis $\varepsilon$ init.	$\varepsilon$	0.1
Spline basis $\mu$ scaling	$\mu$	1.0
Basis activation scaling	$\sigma_b$	1.0
Basis spline scaling	$\sigma_s$	1.0
Initial basis param.	$\tau_0$	1.0
Train basis param.	$\tau_{\text{trainable}}$	true
GaussQuad_nodes	$N_{\text{quad}}$	200
Use mixture prior	(-)	false
<b>KAN Likelihood</b>		
hidden_widths	$q, 2q + 1$	81, 162
All other KAN hparams	Identical to EBM Prior	
generator_noise	$\sigma_{\varepsilon}$	0.1
generator_variance	$\sigma_{\text{llhood}}$	0.1
output_activation	$\sigma_{\text{act}}$	sigmoid
Importance sampling resampler	resampler	residual
ESS threshold	$\gamma$	0.5
<b>Grid updating</b>		
update_prior_grid	(-)	true
update_llhood_grid	(-)	true
num_grid_updating_samples	(-)	100
grid_update_frequency	(-)	100
grid_update_decay	(-)	0.999
<b>Training</b>		
batch_size	$N_x$	100
importance_sample_size	$N_s$	100
Training examples	$N_{\text{train}}$	50,000
Testing examples	$N_{\text{test}}$	100
num_generated_samples	(-)	3,000
Number of epochs	$N_{\text{epochs}}$	10
eps	$\epsilon$	0.001
<b>Optimizer</b>		
type	(-)	adam
learning_rate	$\eta_{LR}$	0.001
betas	(-)	(0.9, 0.999)

Table 5: Hyperparameters for Sec. 3.2.

<b>EBM Prior</b>		
layer_widths	$p, q$	See Sec. A.6.1
spline_type	(-)	RBF
spline_activation	(-)	Relu
layer_norm	(-)	false
quadrature_method	(-)	gausslegendre
spline_degree	$d$	3
grid_size	$N_{\text{grid}}$	20
grid_update_ratio	$\alpha_{\text{grid}}$	N/A
Initial grid_range (before grid updating)	$[z_{\text{min}}, z_{\text{max}}]$	$[-1, 1]$
Spline basis $\varepsilon$ init.	$\varepsilon$	0.1
Spline basis $\mu$ scaling	$\mu$	1.0
Basis activation scaling	$\sigma_b$	1.0
Basis spline scaling	$\sigma_s$	1.0
Initial basis param.	$\tau_0$	1
Train basis param.	$\tau_{\text{trainable}}$	true
GaussQuad_nodes	$N_{\text{quad}}$	200
Use mixture prior	(-)	true
<b>KAN Likelihood</b>		
cnn_widths	(-)	See Sec. A.6.1
All other KAN hparams	N/A, an MLP CNN was used	
generator_noise	$\sigma_\varepsilon$	0.1
generator_variance	$\sigma_\varepsilon$	0.3
output_activation	$\sigma_{\text{act}}$	sigmoid
Importance sampling resampler	resampler	Not used
ESS threshold	$\gamma$	N/A
VGG16 perceptual loss scale, perceptual_scale	(-)	N/A
<b>Grid updating</b>		
update_prior_grid	(-)	true
update_llhood_grid	(-)	false
num_grid_updating_samples	(-)	100
grid_update_frequency	(-)	100
grid_update_decay	(-)	0.999
<b>Training</b>		
batch_size	$N_x$	50
importance_sample_size	$N_s$	N/A
Training examples	$N_{\text{train}}$	20,000
Testing examples	$N_{\text{test}}$	100
num_generated_samples	(-)	3,000
Number of epochs	$N_{\text{epochs}}$	40
eps	$\epsilon$	0.001
Use VGG16 perceptual loss, use_perceptual_loss	(-)	false
<b>Optimizer</b>		
type	(-)	adam
learning_rate	$\eta_{LR}$	0.0001
betas	(-)	(0.9, 0.999)
<b>POSTERIOR LANGEVIN</b>		
iters	$N_{\text{local}}$	40
step_size	$\eta$	0.01
<b>THERMODYNAMIC INTEGRATION</b>		
iters	$N_{\text{local}}$	(see posterior langevin)
num_temps	$N_t$	5
Initial exponent in power law schedule	$p_{\text{start}}$	2
Final exponent in power law schedule	$p_{\text{end}}$	0.5
Number of cosine cycles	$N_{\text{cycles}}$	0

## A.6.1 SVHN &amp; CELEBA ARCHITECTURES

Table 6: The dense RBF KAN network used as the mixture prior model

Layer	Operation	Output Dim.
Input	Sample $z$	$p = 40$
Energy functions	Dense(40)	$q = 81$

sizes=[40,81]

Table 7: CNN Generator Architecture for SVHN ( $32 \times 32$ )

Layer	Operation	Output Shape	Stride
Input	Latent vector $z$ reshaped	$1 \times 1 \times q$	–
1	$4 \times 4$ convT(256), LeakyReLU	$4 \times 4 \times 256$	1
2	$4 \times 4$ convT(128), LeakyReLU	$8 \times 8 \times 128$	2
3	$4 \times 4$ convT(64), LeakyReLU	$16 \times 16 \times 64$	2
4	$4 \times 4$ convT(3), Sigmoid	$32 \times 32 \times 3$	2

Config: kernel=4,4,4,4 strides=1/2/2/2, paddings=0/1/1/1, activation=LeakyReLU, batchnorm=False

Table 8: CNN Generator Architecture for CelebA ( $64 \times 64$ )

Layer	Operation	Output Shape	Stride
Input	Latent vector $z$ reshaped	$1 \times 1 \times q$	–
1	$4 \times 4$ convT(512), LeakyReLU	$4 \times 4 \times 512$	1
2	$4 \times 4$ convT(256), LeakyReLU	$8 \times 8 \times 256$	2
3	$4 \times 4$ convT(128), LeakyReLU	$16 \times 16 \times 128$	2
4	$4 \times 4$ convT(64), LeakyReLU	$32 \times 32 \times 64$	2
5	$4 \times 4$ convT(3), Sigmoid	$64 \times 64 \times 3$	2

Config: kernel=4,4,4,4,4 strides=1/2/2/2/2, paddings=0/1/1/1/1, activation=LeakyReLU, batchnorm=False